

1 **Validation of Inner Magnetosphere Particle Transport**
2 **and Acceleration Model (IMPTAM) with long-term**
3 **GOES MAGED measurements of keV electron fluxes at**
4 **geostationary orbit**

5 **N. Yu. Ganushkina^{1,2}, I. Sillanpää², D. Welling^{1,3}, J. Haiducek¹, M. Liemohn¹,**
6 **S. Dubyagin², J. V. Rodriguez^{4,5}**

7 ¹University of Michigan, Ann Arbor, Michigan, USA.

8 ²Finnish Meteorological Institute, Earth Observations, Helsinki, Finland.

9 ³University of Texas at Arlington, Arlington, TX, USA

10 ⁴Cooperative Institute for Research in Environmental Sciences, University of Colorado Boulder, Boulder,
11 Colorado, USA.

12 ⁵National Centers for Environmental Information, National Oceanic and Atmospheric Administration,
13 Boulder, Colorado, USA.

14 **Key Points:**

15 • IMPTAM performs well, with the ratio between the GOES MAGED and mod-
16 elled keV electron fluxes at 06 MLT close to one.

17 • Peaks of IMPTAM fluxes are shifted towards midnight due to the background field
18 models and the sources and losses used inside IMPTAM

19 • Error is a factor of two based on median symmetric accuracy with largest differ-
20 ence of one order of magnitude, Heidke skill scores are low

21 **Abstract**

22 Surface charging by keV electrons can pose a serious risk for satellites. There is a
 23 need for physical models with the correct and validated dynamical behavior. 18.5 months
 24 (2013-2015) output from the continuous operation online in real time as a nowcast of the
 25 Inner Magnetosphere Particle Transport and Acceleration model (IMPTAM) is compared
 26 to the GOES 13 MAGED data for 40, 75, and 150 keV energies. The observed and mod-
 27 eled electron fluxes were organized by MLT and IMPTAM driving parameters, the ob-
 28 served IMF B_Z , B_Y , $|B|$, the solar wind speed V_{SW} , the dynamic pressure P_{SW} , and K_p
 29 and SYM-H indices. The peaks for modeled fluxes are shifted towards midnight but the
 30 ratio between the observed and modeled fluxes at around 06 MLT is close to one. All
 31 the statistical patterns exhibit very similar features with the largest differences of about
 32 one order of magnitude at 18-24 MLT. Based on binary event analysis, 20-78% of thresh-
 33 old crossings are reproduced but Heidke skill scores are low. The modeled fluxes are off
 34 by a factor of two in terms of the median symmetric accuracy. The direction of the er-
 35 ror varies with energy: overprediction by 50% for 40 keV, overprediction by two for 75
 36 keV, and underprediction by 18% for 150 keV. The revealed discrepancies are due to the
 37 boundary conditions developed for ions but used for electrons, absence of substorm ef-
 38 fects, representations of electric and magnetic fields which can result in not enough adi-
 39 abatic acceleration, and simple models for electron lifetimes.

40 **1 Introduction**

41 According to the Index of Objects Launched into Outer Space (<http://www.unoosa.org/oosa/osoindex/>)
 42 maintained by the United Nations Office for Outer Space Affairs (UNOOSA), there were
 43 about 1980 active satellites in orbit in April 2018. Many of them traverse the variable
 44 radiation environment in the magnetosphere. One of the primary constituents of the ra-
 45 diation environment is the electrons with energies ranging from 1 to tens of keVs. One
 46 obvious example of their importance is their role as the seed population, being further
 47 accelerated to MeV energies by various processes in the Earth's radiation belts (e.g., Horne
 48 et al., 2005; Y. Chen et al., 2007; Li et al., 2014; Jaynes et al., 2015; Boyd et al., 2016).
 49 At the same time, plasma sheet electron and ion distributions get altered into unstable
 50 forms, exciting various plasma waves (notably VLF chorus and EMIC waves) that can
 51 either energize or scatter relativistic particles (Kennel & Petschek, 1966; Kennel & Thorne,
 52 1967; Green & Kivelson, 2001, 2004; Y. Chen et al., 2006; Shprits et al., 2006; Usanova
 53 et al., 2014; Foster et al., 2017). MeV electrons are one of the major sources of damag-
 54 ing space weather effects on space assets inside the radiation belts (see, for example, Baker
 55 et al. (2018) and references therein).

56 The electrons with energies of 10's of keVs do not penetrate deep into the satel-
 57 lite materials but stay near the surface, posing a serious risk for satellites in the form
 58 of surface charging (Garrett, 1981; Lanzerotti et al., 1998; Davis et al., 2008; Thomsen
 59 et al., 2013). The electron fluxes at these keV energies vary significantly with geomag-
 60 netic activity on the scale of minutes or even shorter. Their dynamics is determined by
 61 convective and substorm-associated electric fields in the magnetosphere (Mauk & Meng,
 62 1983; Kerns et al., 1994; Liemohn et al., 1998; Ganushkina et al., 2013, 2014). When a
 63 satellite anomaly due to surface charging occurs, the radiation environment may be more
 64 extreme than that given by the specification models used for design (Iucci et al., 2005;
 65 Mato-Vlez et al., 2018). However, data may not be available at the location of the satel-
 66 lite to determine the cause of the anomaly. Thus, there is a need for physical models with
 67 the correct dynamical behavior that can be used to reconstruct the radiation environ-
 68 ment at any location at any satellite orbit. Prediction models of MeV electron fluxes do
 69 daily averaging (Balikhin et al., 2016), even though less than one hour variability is im-
 70 portant for them. This was taken into account in VERB (Subbotin & Shprits, 2009) (<http://rbm.epss.ucla.edu/realtim>
 71 forecast/) and BAS (Glauert et al., 2014) (http://fp7-spacecast.eu/index.php?page=he_forecasts)

72 radiation belt codes, for example. For keV electron fluxes, smaller scale variations do not
 73 allow averaging over an orbit/day/hour and they must be considered while modeling the
 74 fluxes.

75 Several modeling attempts for keV electron dynamics have been made (e.g., Jordanova & Miyoshi, 2005; Miyoshi et al., 2006; Y. Chen et al., 2006; Jordanova et al., 2014)
 76 focusing mainly on the application to specific events. A couple of models, namely, the
 77 Fok Ring Current Model (FRC) (Fok & Moore, 1997; Fok et al., 1999, 2001) and the Com-
 78 prehensive Inner-Magnetosphere Ionosphere (CIMI) model (Fok et al., 2001, 2011, 2014)
 79 run online at the Community Coordinated Modeling Center (CCMC) (<http://ccmc.gsfc.nasa.gov/index.php>)
 80 in near real time but without real time comparison with the observations. The purely
 81 empirical model for electron flux for 1 eV to 40 keV at GEO (Denton et al., 2015, 2016,
 82 2017) based on LANL data (<http://gemelli.spacescience.org/mdlenton/>) and dependent
 83 on the Kp index, daily F10.7 index, and $-V_{SW}B_Z$ is not well suited for modeling of the
 84 specific events and of the fast variations of keV electrons due to its limited number of
 85 driving parameters. Another empirical model, the MSSL Electron Population Model, based
 86 on Cluster PEACE and EFW instrument data from 2001-2014 provides the omni-directional
 87 10 eV to 40 keV electron population parameterised by solar wind velocity and Kp-index
 88 at MEO (L=4-6) and GEO (L=6-7). It is not accessible without registration to the ESA
 89 Space Radiation Expert Service Centre and the resolutions of the grids in MLT, energy,
 90 and driving parameters are quite low. A very different approach is used in the SNB3GEO
 91 models (e.g., Balikhin et al., 2011) (<http://www.ssg.group.shef.ac.uk/USSW/UOSSW.html>)
 92 based on Multi-Input Single-Output (MISO) Nonlinear AutoRegressive Moving Average
 93 with eXogenous inputs (NARMAX) methodologies (Leontaritis & Billings, 1985a,
 94 1985b). Boynton et al. (2016) extended the forecast to lower energies of 30-600 keV elec-
 95 trons using MAGED GOES satellite data which is now shown under the H2020 PROGRESS
 96 project (<https://ssg.group.shef.ac.uk/progress2/html/index.phtml>). In general, it is chal-
 97 lenging to forecast keV electrons one day ahead because the same day variations in the
 98 solar wind affect the current electron flux. In Boynton et al. (2016), the past 24 hour av-
 99 erages for each hour were computed and they represented one hour forecasts but with-
 100 out smaller-time-scale variations.

102 The Inner Magnetosphere Particle Transport and Acceleration model (IMPTAM)
 103 (Ganushkina et al., 2013, 2014, 2015) was developed for low energy (< 200 keV) elec-
 104 trons and has been operating online in real time since February 2013 under the EU-funded
 105 projects (<http://fp7-spacecast.eu>, imptam.fmi.fi) and at <http://csem.ingen.umich.edu/tools/imptam>
 106 with the most recent version running at <https://ssg.group.shef.ac.uk/progress2/html/index.phtml>
 107 and at <http://citrine.ingen.umich.edu/imptam/>. The model covers the whole inner mag-
 108 netosphere from $3 R_E$ up to $10 R_E$ distances. It is driven by the real time solar wind
 109 and IMF parameters and geomagnetic indices and provides the outputs of the keV elec-
 110 tron fluxes at a given time step at all L-shells and at all satellite orbits within the com-
 111 putational domain. So far, the output of IMPTAM is compared with the only data set
 112 available in real time for keV electrons in the inner magnetosphere which is the geosta-
 113 tionary GOES 13 or GOES 15 (whenever available) MAGED data on electron fluxes at
 114 three energies (40, 75, and 150 keV). A preliminary validation study (Ganushkina et al.,
 115 2015) demonstrated that IMPTAM provides a now-cast of keV electrons comparable to
 116 the observations so that the same order of magnitude variations of the observed fluxes
 117 were reproduced. At the same time, the validation study was done only for four months
 118 of IMPTAM performance.

119 The quality of any model is determined by how well this model predicts the quan-
 120 tities being modeled as compared to real data and how much it deviates from the ob-
 121 servations. The direct data-model, or observed-modeled electron flux, comparison alone
 122 cannot fully quantitatively reveal the model performance. There are several metrics to
 123 assess the model's quality. In the validation study by Ganushkina et al. (2015), we com-
 124 puted (1) the Normalized Root-Mean-Squared Deviation (NRMSD) (Walther & Moore,

2005; Wilks, 2006) and the associated standard deviations of the observations and (2) the binary event tables (Jolliffe & Stephenson, 2012) and Heidke Skill Score (HSS) (Heidke, 1926; Doswell III et al., 1990; Balch, 2008) based on them. For four months of IMPTAM performance, the NRMSE ranged from 0.015 to 0.0324 and the hit rates were reasonable (0.159-0.739) with the best hit rate reached for 75 keV electrons (0.367-0.739) but the Heidke Skill Scores were rather small (0.17 and below).

There is a need to evaluate the model performance on larger data sets and with more appropriate metrics. In the case of keV electron fluxes, there are several orders of magnitude differences at different locations along the geostationary orbit and during quiet and disturbed conditions with different levels of variability. Therefore, using of scale-dependent accuracy measures as simple model error or mean error can be problematic, since it can result in very large values due to the outliers in the data and in the model (Morley et al., 2018).

In the present paper we extend the study of Ganushkina et al. (2015) on the performance of IMPTAM by analyzing 18.5 months of IMPTAM output during its continuous operation online in near real time. In Section 2, the GOES 13 MAGED data used in the study are briefly described along with the method of determining the flight direction integrated differential electron fluxes following (Sillanp et al., 2017). Section 3 presents IMPTAM settings and driving parameters (solar wind and IMF parameters and geomagnetic indices) which were kept unchanged during the whole period analyzed in the paper. The comparative analysis of long-term variations of keV electron fluxes modeled by IMPTAM and measured by the GOES 13 MAGED instrument as dependent on IMPTAM driving parameters is given in Section 4. To evaluate quantitatively IMPTAM's overall performance, independent of its driving parameters, the appropriate metrics are introduced and computed in Section 5. The obtained results are discussed and conclusions are given in Section 6.

2 Data for IMPTAM validation: GOES MAGED electron fluxes at geostationary orbit

The only data on keV electrons in the inner Earth's magnetosphere which can be used for comparison with modeled electron fluxes by IMPTAM in real time are the measurements by the geostationary GOES 13 (or GOES 14 and 15, whenever available) MAGED instrument. The MAGED (MAGnetospheric Electron Detector) instrument is a set of nine collimated solid state telescopes (Hanser, 2011; Rowland & Weigel, 2012). The nine detectors, or telescopes, each with a 30° full-angle conical field-of-view, form a cruciform field-of-regard with the central telescope 1 pointing anti-Earthward. Each telescope measures electron fluxes in five energy channels of 30-50 keV, 50-100 keV, 100-200 keV, 200-350 keV, and 350-600 keV. The MAGED archival data are provided as directional differential electron fluxes in units of $cm^{-2} sec^{-1} sr^{-1} keV^{-1}$ determined for the midpoint of the five energy ranges (i.e., at 40, 75, 150, 275, and 475 keV) and given separately for all nine telescopes, as well as the pitch angles calculated from the GOES Magnetometer 1 data (Rodriguez, 2014). We consider the first three energy channels. Using electron fluxes measured by separate telescopes provides sparse information on the full distribution function at the GOES location, although they can be used to estimate the complete pitch-angle distribution (Hartley et al., 2013). Coverage of pitch angles of electrons entering a certain telescope varies with time, magnetic field changes being one of the reasons for that. Instead of determining the pitch angles measured by separate telescopes and using the corresponding fluxes of nine separate values from the nine telescopes, we compute one omni-directionally averaged flux value for each of the energies of 40 keV, 75 keV, and 150 keV, flight direction integrated differential electron fluxes, following the method presented in (Sillanp et al., 2017). Here, we briefly summarize the procedure.

Several assumptions are made when computing the flight direction integrated differential electron flux, namely, that the directional electron fluxes are (1) cylindrically symmetric with respect to the direction of the magnetic field (i.e., fluxes are uniform in all directions with the same pitch angle) and (2) symmetrically reflected with respect to the plane perpendicular to the magnetic field (i.e., fluxes for pitch angles α from 0° to 90° are the same as from 90° to 180° , $J(180^\circ - \alpha) = J(\alpha)$).

The flight direction integrated differential electron flux for each energy channel can be computed using the directional differential electron fluxes of individual telescopes in order to get the differential fluxes in all directions, then, integrating these fluxes over the full solid angle of 4π . To avoid the confusion which may arise due to differences in units for the computed flight direction integrated differential electron fluxes (Roberts, 1965), the directional differential electron fluxes provided by separate telescopes and fluxes modeled by IMPTAM, we obtain the flight direction integrated differential electron flux J in units of $cm^{-2} sec^{-1} sr^{-1} keV^{-1}$ by normalizing the computed values by 4π :

$$J = \frac{1}{4\pi} \int_{4\pi} J(\Omega) d\Omega = \frac{1}{4\pi} \cdot 2 \cdot 2\pi \int_0^{\pi/2} J(\alpha) \sin(\alpha) d\alpha = \\ = \sum_{i=1}^n J_i \int_{\alpha_{i0}}^{\alpha_{i1}} \sin(\alpha) d\alpha = \sum_{i=1}^n J_i [-\cos(\alpha_{i0}) - (-\cos(\alpha_{i1}))], \quad (1)$$

where

$$J_i = \frac{\sin(\alpha_{i0}) \cdot J_{i0} + \sin(\alpha_{i1}) \cdot J_{i1}}{\sin(\alpha_{i0}) + \sin(\alpha_{i1})}, \quad (2)$$

and $J(\Omega)$ is the directional flux as a function of the solid angle Ω , J_i is the differential flux for each pitch angle interval i which is the actual pitch angles of the telescopes, J_{i0} is the differential flux by a detector at the beginning of a pitch angle interval i and J_{i1} is the differential flux at the end of the interval with the corresponding pitch angles α_{i0} and α_{i1} , respectively.

In the present study we use the GOES 13 MAGED data of electron fluxes and the data for the pitch angles of each telescope with 5 minute averaging from <http://satdat.ngdc.noaa.gov/sem/goes/data/>

3 IMPTAM setup for modeling of keV electron fluxes at GOES 13 locations

The Inner Magnetosphere Particle Transport and Acceleration Model (IMPTAM), version for electrons (Ganushkina et al., 2013, 2014, 2015), traces distributions of electrons in the drift approximation (1st and 2nd adiabatic invariants conserved) with arbitrary pitch angles from the plasma sheet (starting at $10 R_E$) to the inner L-shell regions ($3 R_E$) with energies reaching up to hundreds of keVs in time-dependent magnetic and electric fields. We obtain the changes in the electron distribution function $f(R, \phi, t, E_{kin}, \alpha)$, where R and ϕ are the radial and azimuthal coordinates in the equatorial plane, respectively, t is the time, E_{kin} is the particle energy, and α is the particle pitch angle, considering the drift velocity as a combination of the $\mathbf{E} \times \mathbf{B}$ drift velocity and the velocities of gradient and curvature drifts. Even the grid for distance is in R , the L -values are computed inside IMPTAM. Liouville's theorem is used to gain information of the entire distribution function with losses taken into account. For electron losses, we consider the convection outflow and pitch angle diffusion. In IMPTAM we do not use the pitch angle diffusion coefficients directly, but electron lifetimes computed from them. When running IMPTAM online in real time, we used two model representations for the electron lifetimes τ , one of M. W. Chen et al. (2005) at distances from $10 R_E$, where our IMPTAM outer boundary was located, to $6 R_E$ and the other of Shprits et al. (2007) at distances from $6 R_E$ to $3 R_E$, which was the IMPTAM inner boundary. The M. W. Chen et al. (2005) representation does not include any dependence on the geomagnetic activity but it includes an MLT-dependence and it can be applied when we model electron

222 motion from the plasma sheet to geostationary orbit. The Shprits et al. (2007) repre-
 223 sentation does not include an MLT-dependence but it includes the Kp-dependence which
 224 is important when we apply these electron lifetimes at distances inside geostationary or-
 225 bit. Shprits et al. (2007), and addressed only interactions due to chorus waves, hiss waves
 226 are not taken into account but this is acceptable for the comparison between the mod-
 227 eled and observed electron fluxes at geostationary orbit. For the obtained distribution
 228 function, we apply radial diffusion by solving the radial diffusion equation (Schulz & Lanze-
 229 rotti, 1974). Kp-dependent radial diffusion coefficients D_{LL} for the magnetic field fluc-
 230 tuations are computed following Brautigam and Albert (2000). After that, we repeat the
 231 order of calculation: first, we solve transport with losses and then apply the diffusion.
 232 More detailed description of IMPTAM is given in Ganushkina et al. (2014) and Ganushkina
 233 et al. (2015).

234 The IMPTAM nowcast (imptam.fmi.fi) for low energy (1-200 keV) electrons in the
 235 inner magnetosphere has been operating online since February 2013 in near-real time un-
 236 der the FP7 SPACECAST (<http://fp7-spacecast.eu>), SPACESTORM (<http://www.spacestorm.eu/>)
 237 and H2020 PROGRESS (<https://ssg.group.shef.ac.uk/progress2/html/>) projects funded
 238 by the European Commission. Real time geostationary GOES 13 MAGED data on elec-
 239 tron fluxes for three energies of 40, 75 and 150 keV have been used for comparison and
 240 validation of IMPTAM running online (Ganushkina et al., 2015). IMPTAM is driven by
 241 the solar wind and IMF parameters and geomagnetic indices obtained in real time.

242 Inside IMPTAM, the set of models which was found to provide best agreement with
 243 the measured electron fluxes at geostationary orbit is used, namely, (1) a dipole model
 244 for the internal magnetic field, (2) T96 model (Tsyganenko, 1995) for the external mag-
 245 netic field, and (3) (Boyle et al., 1997) polar cap potential mapped to the magnetosphere.
 246 The T96 model uses the Dst index, solar wind pressure P_{SW} , and IMF B_Y and B_Z com-
 247 ponents as input parameters. We re-compute the magnetic field configuration in the en-
 248 tire modeling domain every 5 minutes using the observed, 5 minute-averaged P_{SW} and
 249 IMF B_Y and B_Z and, instead of hourly Dst index, we use 5 minute SYM-H index for
 250 consistency with other parameters. Wanliss and Showalter (2006) showed that the Dst
 251 and SYM-H indices correlate with a coefficient higher than 0.9, indicating that they can
 252 be used interchangeably. Furthermore, Katus and Liemohn (2013) demonstrated that,
 253 during storm times, these indices are close to each other but can vary from each by up
 254 to 20%. This is an acceptable difference that allows for a higher-time resolution of this
 255 input parameter to the T96 model. The electric field (Boyle et al., 1997) is determined
 256 using the solar wind speed V_{SW} , the IMF strength $|B|$ and its components B_Y and B_Z
 257 (via IMF clock angle θ_{IMF}) dependent on radial distance and MLT. We set the model
 258 boundary at 10 R_E and use the kappa electron distribution function. Parameters of the
 259 kappa distribution function are the number density n and temperature T in the plasma
 260 sheet given by the empirical model derived from Geotail data by (Tsyganenko & Mukai,
 261 2003). In IMPTAM simulation, the electron n is assumed to be the same as that for ions
 262 in the model, but $T_e/T_i = 0.2$ is taken into account. The (Tsyganenko & Mukai, 2003)
 263 model uses as input parameters the solar wind speed V_{SW} and density N_{SW} as well as
 264 the B_Z component of IMF. Kp-index is a parameter for the radial diffusion coefficients
 265 (D_{LL} and (Shprits et al., 2007) electron lifetimes. Thus, the IMPTAM driving param-
 266 eters are (1) the IMF B_Z and (2) B_Y components, (3) the IMF strength $|B|$, (4) the so-
 267 lar wind speed V_{SW} and (5) dynamic pressure P_{SW} , (6) Kp and (7) SYM-H indices. These
 268 parameters are of primary interest in data-model comparison. The comparison between
 269 the keV electron fluxes modeled by IMPTAM and measured by GOES 13 MAGED in-
 270 strument presented here is for the period from 20 September 2013 (by then, the initial
 271 checks of IMPTAM running online which started in February 2013 were done) to 31 March
 272 2015. During this period, the model's settings were not changed. For the IMPTAM in-
 273 put parameters, we used the openly available ACE data (<http://services.swpc.noaa.gov/text/>)
 274 together with data from OMNIWeb (<http://omniweb.gsfc.nasa.gov/>) and the World Data
 275 Center for Geomagnetism, Kyoto (<http://wdc.kugi.kyoto-u.ac.jp/wdc/Sec3.html>).

276 **4 Comparative analysis of long-term variations of keV electron fluxes**
 277 **modeled by IMPTAM and measured by GOES 13 MAGED instru-**
 278 **ment at geostationary orbit**

279 We use the 5 minute averaging for GOES 13 MAGED data and the 5 minute IMP-
 280 TAM output as flight-direction integrated differential fluxes for energies of 40, 75, and
 281 150 keV that are directly comparable during the period between September 20, 2013 and
 282 March 31, 2015. The direct data-model comparison during two periods, two months of
 283 July-August 2013 and four months of January-April 2014 was analyzed in Ganushkina
 284 et al. (2015). Time series of the observed and modeled fluxes over a 18.5 months period
 285 are presented in Figure 1 together with IMPTAM driving parameters. Since keV elec-
 286 tron fluxes vary at rather short time scales, the conclusions which can be made from this
 287 Figure 1 are limited to the following:

288 (1) the modeled 40 keV electron fluxes vary within the range observed by GOES
 289 13 MAGED but, at the same time, sharp dropouts are not reproduced;
 290 (2) the modeled 75 keV electron fluxes have a narrower range than observed, but
 291 fail to fit the dropouts and smaller fluxes;
 292 (3) in general, statement (2) is true also for 150 keV electrons.

293 Looking at this Figure 1, it is very difficult to make any conclusions about the in-
 294 fluence of driving parameters upon the modeled fluxes. Therefore, we analyze in details
 295 the observed and modeled electron fluxes organized by MLT along the GOES 13 orbit
 296 and the IMPTAM driving parameters (IMF B_Z , B_Y components and strength $|B|$, V_{SW}
 297 and P_{SW} , K_p and SYM-H), instead of direct data-model comparison for the modeled
 298 period. This approach can provide more insights into the influence of the different pa-
 299 rameters on the IMPTAM performance quality. Figures 2-8 present the comparison re-
 300 sults. The MAGED electron fluxes (panels (a), (d), and (g)) and the IMPTAM modeled
 301 electron fluxes (panels (b), (e), and (h)) for the three energies of 40, 75, and 150 keV are
 302 plotted in the same logarithmic scale. Panels (c), (f), and (i) present the ratio between
 303 the modeled and observed fluxes in the logarithmic scale. Bottom panel (j) shows the
 304 data counts for the occurrence of a corresponding driving parameter.

305 Figure 2 shows the modeled (panels on the left) and the observed (panels in the
 306 middle) electron fluxes binned by MLT with 1 hour step and IMF B_Z with 1 nT step.
 307 The fluxes were computed as the average fluxes from all datapoints which fall into cer-
 308 tain bins but plotted in the logarithmic scale. In addition, the ratio between the mod-
 309 eled and observed fluxes, after averaging those fluxes in each bin, is shown in panels on
 310 the right, also plotted in logarithmic scale. The way how this ratio was computed, when
 311 one average (of modeled fluxes in a bin) was divided by another average (of observed fluxes
 312 in a bin), results in higher fluxes being given more weight in it. The ratio of the aver-
 313 aged values ($\frac{\sum IMPTAMflux}{\sum GOESflux}$) will not be equal to the averaged ratio of the same val-
 314 ues ($\frac{\sum IMPTAMflux}{\sum GOESflux}$) in which lower fluxes will have more influence. In our present study,
 315 we compute the ratio between the averaged values, since we wanted to focus on the abil-
 316 ity of IMPTAM to reproduce the higher fluxes which can be reached by keV electrons
 317 at the geostationary orbit. This focus is due to the fact that the surface potential of a
 318 spacecraft can become significant ranging from several to ten kV as long as electron fluxes
 319 exceed a spacecraft-dependent threshold level. For specific spacecraft and their surfaces,
 320 certain electron energies are of most importance and the threshold depends on them. For
 321 example, at the LANL satellites, the most important energies for surface charging were
 322 found to be ranging from 5 to 50 keV (Thomsen et al., 2013; Mato-Vlez et al., 2018). For
 323 GOES, we do not possess readily such information, therefore, the range of higher fluxes,
 324 observed and modeled, was given special attention here and the ratio was computed be-
 325 tween the averaged values.

326 Since this Figure 2 contains all the points with corresponding IMF B_Z values, Fig-
 327 ure 2j gives the distribution of data counts within the observed range of MLT and IMF

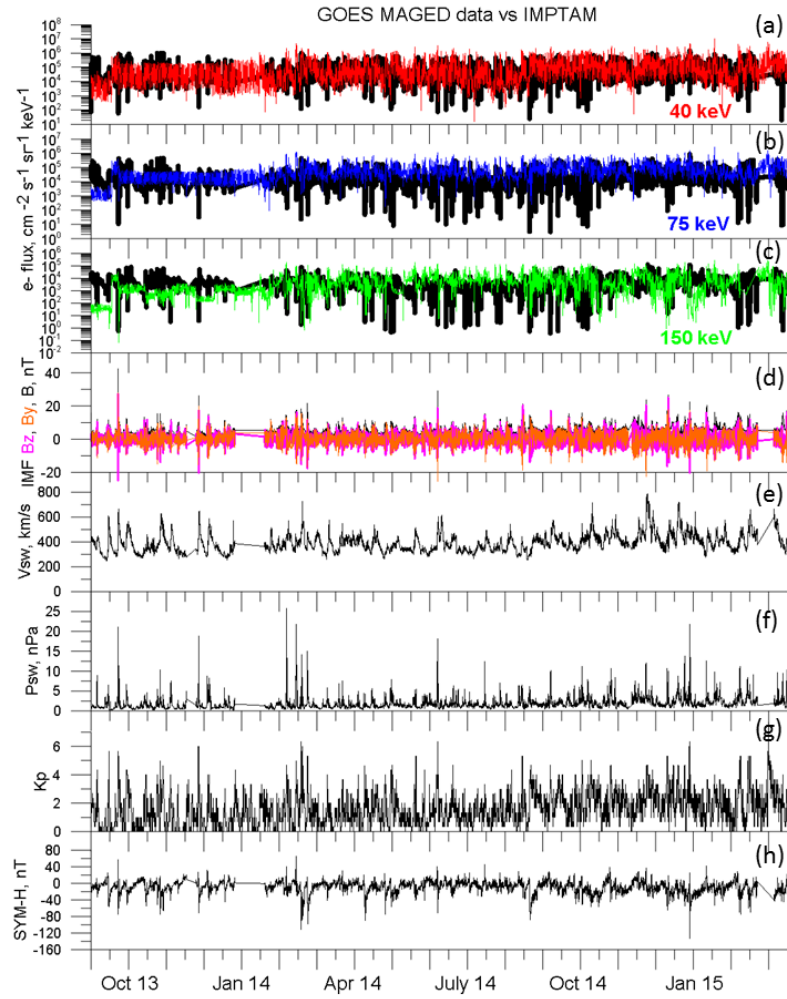


Figure 1. IMPTAM performance run in real time: the observed fluxes (black lines) at GOES 13 together with the modeled fluxes for (a) 40 keV (red line), (b) 75 keV (blue line), and (c) 150 keV electrons (green line) with model driving parameters as observed (d) IMF Bz (pink line), By (orange line) and B (black line), (e) solar wind velocity, and (f) solar wind dynamic pressure and geomagnetic indices (g) Kp and (h) SYM-H.

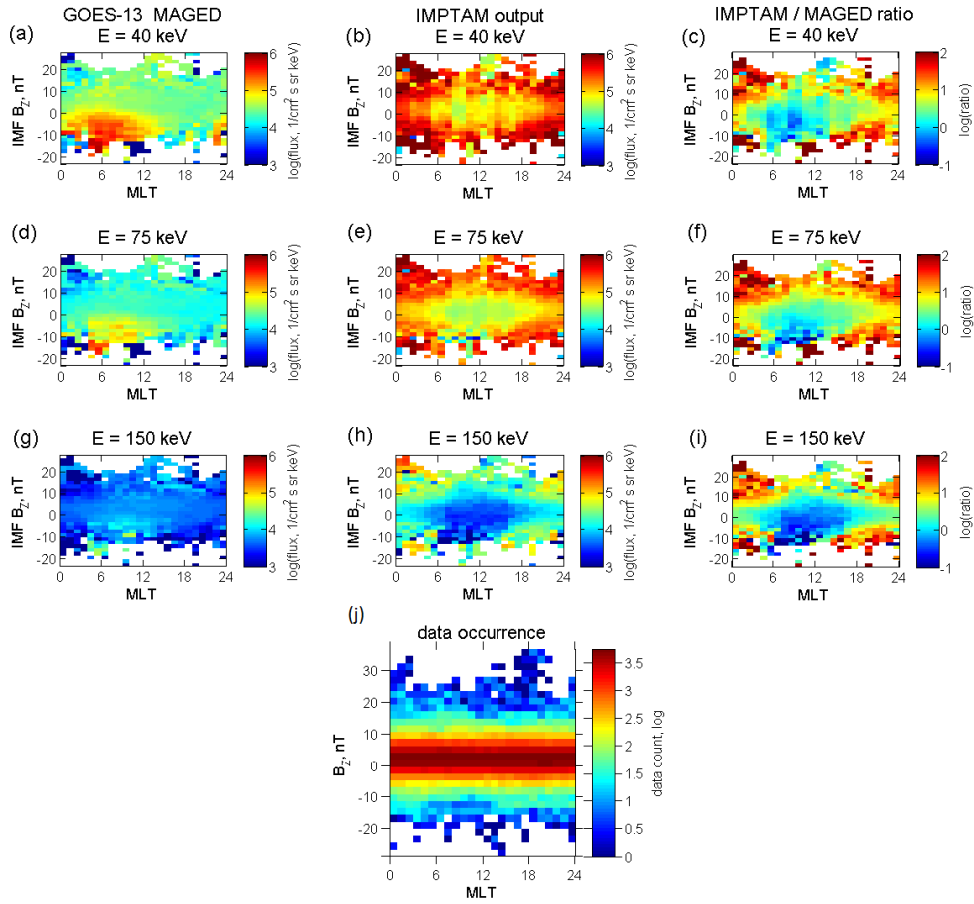


Figure 2. Flight-direction integrated differential electron fluxes in logarithmic scale for the energies of 40, 75, and 150 keV computed from the GOES 13 MAGED data (panels (a), (d), and (g)) and modeled by the IMPTAM (panels (b), (e), and (h)) binned by MLT and IMF B_Z , and then averaged, together with the ratio between them in logarithmic scale (panels (c), (f), and (i)). Bottom panel (j) shows the data counts for the IMF B_Z occurrence.

328 B_Z . From Figure 2j, we can see that the maximum occurrence of data points is for IMF
 329 B_Z from 0 to +5 nT with about 10^4 points per bin and all points above +10 nT and be-
 330 low -8 nT constitute less than 10% of the maximum number of points in that MLT range.
 331 Points with IMF B_Z above +20 nT and below -15 nT are already less than 1% of the
 332 maximum number of points. Therefore, for our analysis, the main attention will be paid
 333 to the modeled and observed fluxes which fall into the IMF B_Z range of -10 to 10 nT
 334 (same absolute values for negative and positive B_Z are chosen to make the analysis of
 335 Figure 2 easier).

336 The observed 40 keV electron fluxes (Figure 2a) exhibit the clear peak reaching to
 337 $10^6 \text{ cm}^{-2} \text{ sec}^{-1} \text{ sr}^{-1} \text{ keV}^{-1}$ for negative IMF B_Z (0 to -10 nT) located at a rather wide
 338 midnight-dawn-noon sector of 00-12 MLT. The 40 keV electron flux for positive IMF B_Z
 339 in this MLT sector and for all values of IMF B_Z in the noon-dusk-midnight sector is about
 340 the same, being of $5-8 \cdot 10^4 \text{ cm}^{-2} \text{ sec}^{-1} \text{ sr}^{-1} \text{ keV}^{-1}$. For higher energies the pattern
 341 of electron flux dependence on MLT and IMF B_Z is very similar with fluxes being lower.
 342 The peak values for 75 keV electrons (Figure 2d) are around $5 \cdot 10^5 \text{ cm}^{-2} \text{ sec}^{-1} \text{ sr}^{-1} \text{ keV}^{-1}$
 343 and for 150 keV electrons (Figure 2g) they are about $5 \cdot 10^4 \text{ cm}^{-2} \text{ sec}^{-1} \text{ sr}^{-1} \text{ keV}^{-1}$
 344 and located on the dawn sector. In general, the observed geostationary keV electron fluxes
 345 are very clearly organized by IMF B_Z with maximum fluxes located at around 06 MLT.

346 One particular location of higher observed fluxes can be seen very close to 04-06
 347 MLT for IMF B_Z of about -18 to -12 nT. Comparing this location to the number of data
 348 points presented in Figure 2j tells us that such high fluxes can be the result of averag-
 349 ing over a small number of points where higher values of the observed fluxes get larger
 350 weights. This can be unrealistic and very different if there would have been more, sta-
 351 tistically valuable data points. The same is true for smaller peaks seen at 12-16 MLT
 352 for IMF B_Z above 20 nT.

353 Keeping in mind the number of actual data points corresponding to different IMF
 354 B_Z is especially important when analyzing the modeled fluxes. If we concentrate at the
 355 range of -10 to 10 nT of IMF B_Z , it can be seen that the modeled electron fluxes have
 356 similar peaks for negative IMF B_Z (Figures 2b, e and h) but the maxima of the peaks
 357 are located not at around 06 MLT as observed but shifted towards midnight being be-
 358 between 00 and 06 MLT. The modeled fluxes have peaks at large (> 10 nT) positive IMF
 359 B_Z at around 18-06 MLT for all three energies which are not seen in the observed fluxes.
 360 At the locations of these peaks, the difference of one to two orders of magnitude can be
 361 seen (Figures 2c, f and i). As was stated above, this is the IMF B_Z range where the num-
 362 ber of data points was less than 10% of the maximum number of points in that MLT range.
 363 For negative IMF B_Z , the ratio can also reach one to two orders of magnitude but it is
 364 mainly for IMF B_Z below -10 nT. At the same time, the ratio between the modeled and
 365 the observed fluxes at 00-12 MLT where the observed peak is located is close to one and
 366 up to 10 for several values of IMF B_Z for the presented statistics.

367 In a similar way as presented in Figure 2, Figure 3 shows the modeled and the ob-
 368 served electron fluxes binned by MLT and IMF B_Y , and then averaged, together with
 369 the ratio between them and the distribution of data counts within the observed range
 370 of MLT and IMF B_Y . Following the same estimates as for Figure 2j, we can say that all
 371 points above +12 nT and below -10 nT constitute less than 10% of the maximum num-
 372 ber of points in any given MLT range, so our analysis is concentrated at the range be-
 373 tween -10 and +10 nT for IMF B_Y . The observed 40 keV electron fluxes (Figure 3a) show
 374 the x-shaped peak, again located at around 06 MLT, with values of about $5 \cdot 10^5 \text{ cm}^{-2} \text{ sec}^{-1} \text{ sr}^{-1} \text{ keV}^{-1}$.
 375 The peak widens in MLT (from midnight to noon) with the increase of negative and pos-
 376 itive values of IMF B_Y in magnitude being narrower (± 2 hours from 06 MLT) for IMF
 377 B_Y close to zero. Similar peaks, but an order of magnitude lower and shifted a little more
 378 towards noon than the previous ones, are visible for 75 keV (Figure 3d) and 150 keV elec-
 379 trons (Figure 3g). The modeled fluxes exhibit very similar x-shaped structure but shifted
 380 towards midnight (Figures 3b, e, and h). Due to this shift, the modeled fluxes are one

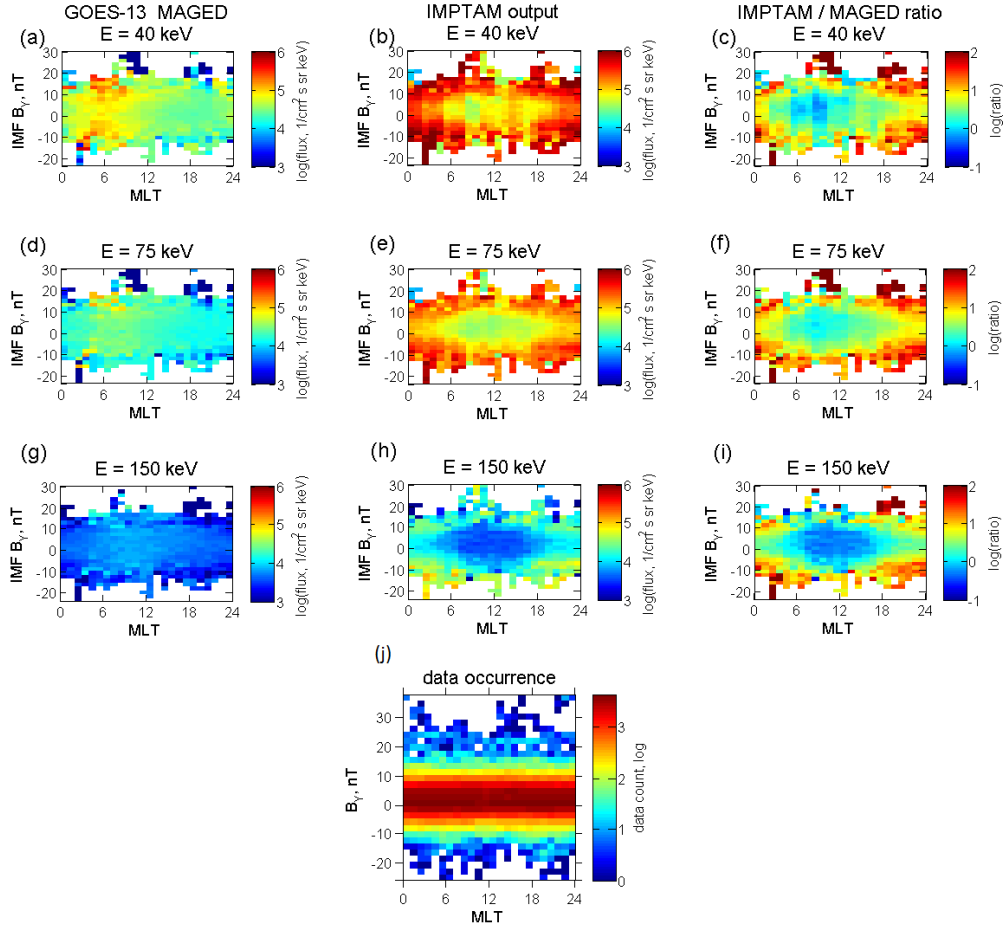


Figure 3. Similar to Figure 2 but the observed and modeled electron fluxes are binned by MLT and IMF B_Y and then averaged with IMF B_Y data occurrence.

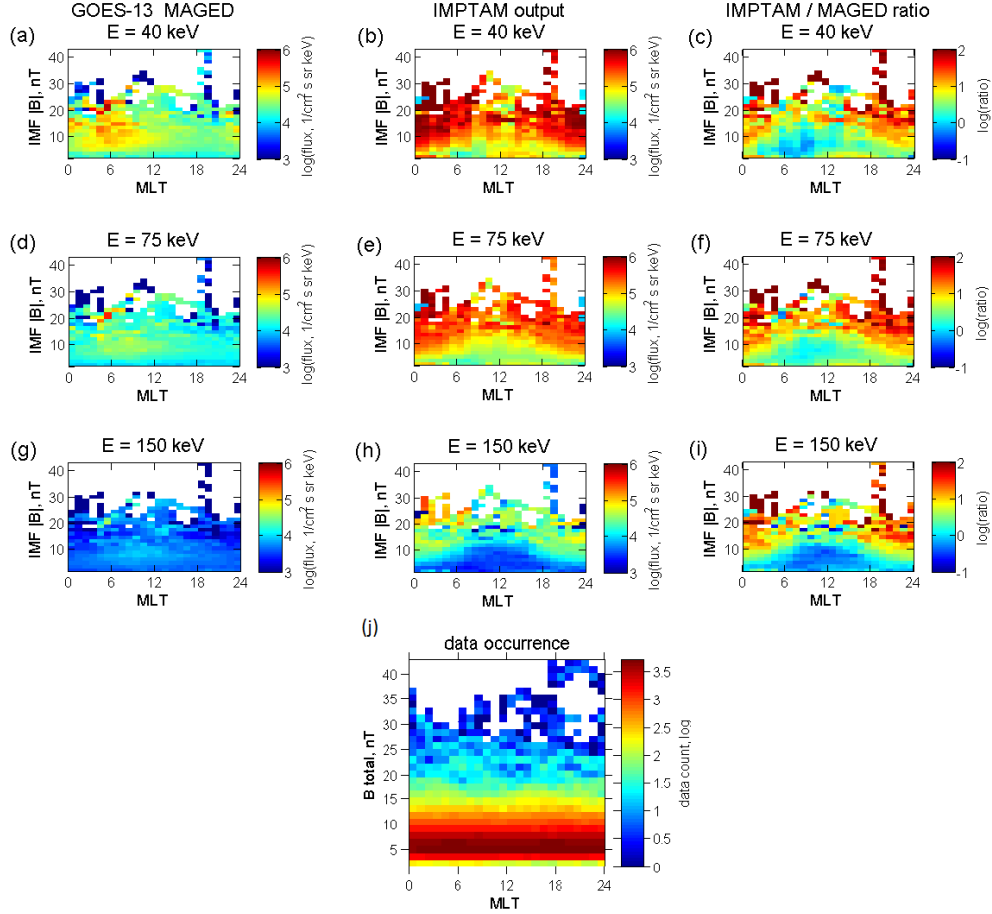


Figure 4. Similar to Figure 2 but the observed and modeled electron fluxes are binned by MLT and IMF $|B|$ and then averaged with IMF $|B|$ data occurrence.

to two orders of magnitude higher than the observed ones at around 18-02 MLT for both positive and negative IMF B_Y values. At 06-12 MLT the ratio is close to one or smaller indicating the difference in fluxes with the modeled smaller than the observed up to one order in magnitude (Figures 3c, f, and i).

Figure 4 presents the modeled and observed electron fluxes binned by MLT and IMF total strength $|B|$, and then averaged, together with the ratio between them and the distribution of data counts within the observed range of MLT and IMF $|B|$. Figure 4j indicates that the data-model comparison needs to be done for IMF $|B|$ below about 20 nT. The observed fluxes show quite similar features as in Figure 2 with peaks at 00-12 MLT but with inverted-V shapes and with an order of magnitude lower and shifted more towards noon than the previous ones with energy (Figures 4a, d, g). The modeled fluxes can reach of one to two orders of magnitude difference at 18-06 MLT for larger (10 to 20 nT) values of IMF $|B|$ (Figures 4b, e, h) but at 06-12 MLT for IMF $|B| < 15$ nT, the ratio between them and the observed ones is close to one (Figures 4c, f, i).

Figure 5 presents the modeled and observed electron fluxes binned by MLT with 1 hour step and solar wind speed V_{SW} with 20 km/s step, and then averaged, together with the ratio between them and the distribution of data counts within the observed range of MLT and V_{SW} . Based on Figure 5j, datapoints with corresponding V_{SW} above 700

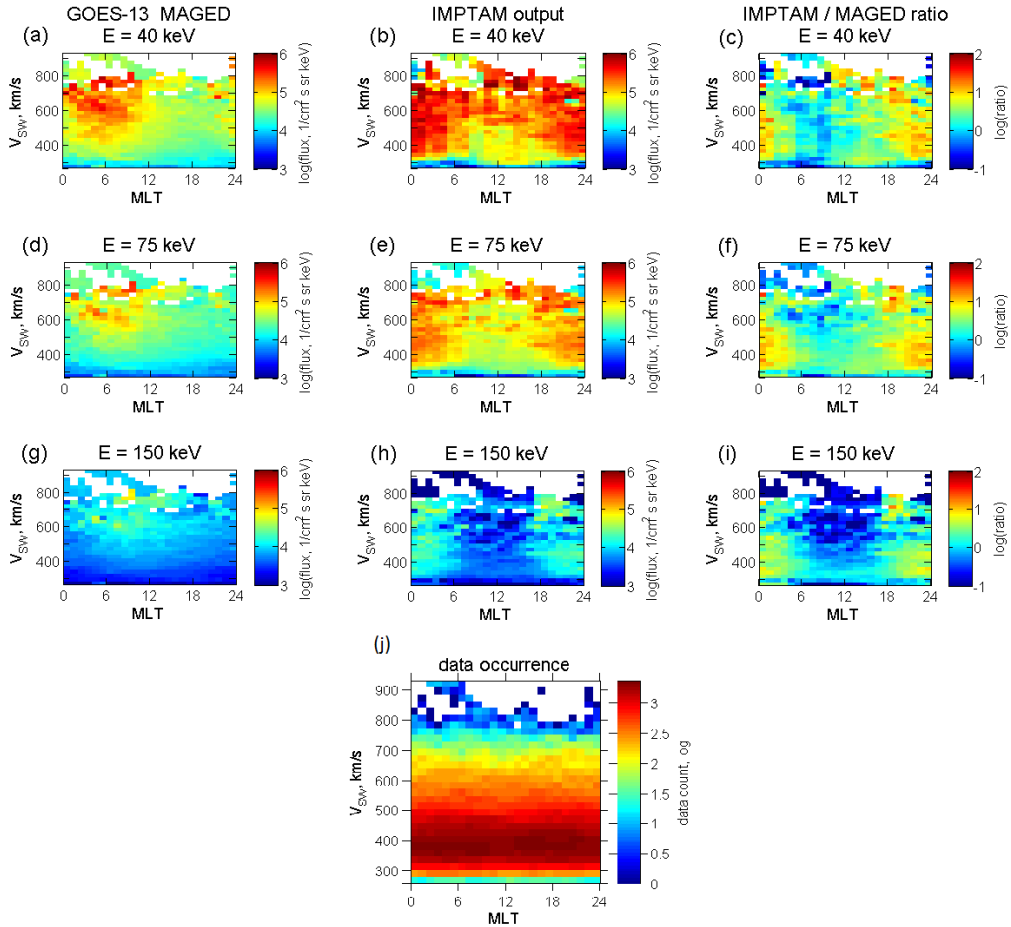


Figure 5. Similar to Figure 2 but the observed and modeled electron fluxes are binned by MLT and solar wind speed V_{SW} and then averaged with V_{SW} data occurrence.

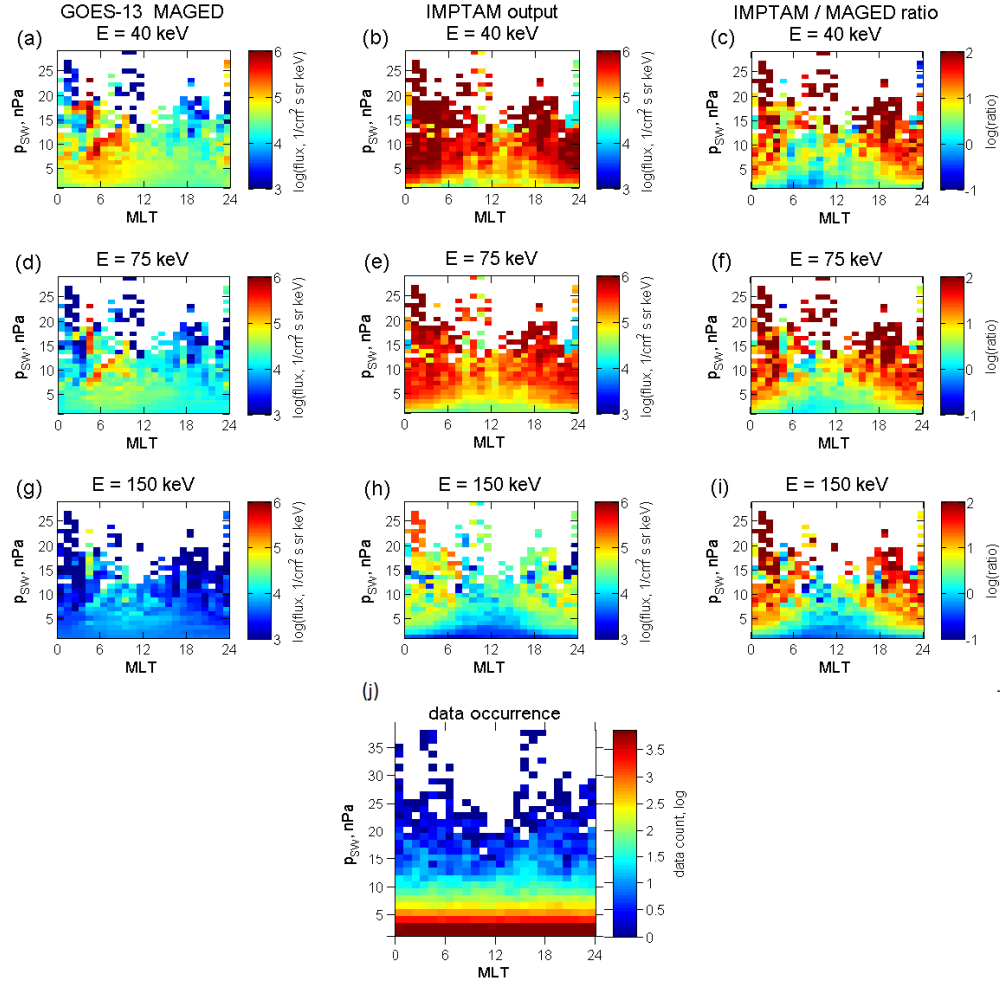


Figure 6. Similar to Figure 2 but the observed and modeled electron fluxes are binned by MLT and solar wind dynamic pressure P_{SW} and then averaged with P_{SW} data occurrence.

km/s constitute less than 10% from the maximum number of points per bin and the corresponding structures in the observed and modeled fluxes can be disregarded. The U-shaped peaks in the observed electron fluxes are located at 00-12 MLT as in previous figures and the fluxes increase with the increase of V_{SW} covering larger range of MLT. The modeled fluxes of about $5 \cdot 10^5 - 10^6 \text{ cm}^{-2} \text{ sec}^{-1} \text{ sr}^{-1} \text{ keV}^{-1}$ for 40 keV electrons are present at a wider than observed range of MLTs (20 -04) for V_{SW} above 200 km/s. The same is true for 75 keVs but with order of magnitude lower fluxes (or 2 orders of magnitude for 150 keV). Shifts of the peaks to midnight instead of dawn are also present. Looking at the ratio we can see that the modeled fluxes are rather close to the observed ones at 06-12 MLT. The main over-estimation is seen at around midnight with about one order of magnitude.

Figure 6 demonstrates the modeled and observed electron fluxes binned by MLT with 1 hour step and solar wind dynamic pressure P_{SW} with 1 nPa step, and then averaged, together with the ratio between them and the distribution of data counts within the observed range of MLT and P_{SW} . As can be seen in Figure 6j, analyzing the observed and modeled fluxes with P_{SW} above 10 nPa can lead to unreasonable conclusions, since the number of points there is less than 10% from the maximum number of points per

416 bin. The largest observed 40 keV electron fluxes (Figure 6a) are located at 00-12 MLT
 417 peaking at around 06 MLT and increasing with the increase of P_{SW} . Similar features
 418 are seen for 75 and 150 keV electron fluxes (Figures 6d and g) but with peaks shifted
 419 towards noon and with order of magnitude smaller values as in all figures described above.
 420 The modeled fluxes are higher than the observed ones at 18-06 MLT with the difference
 421 reaching about 1.5 orders of magnitude at around midnight and 18 MLT. Again, in the
 422 MLT sector of 06-12 for $P_{SW} < 10$ nPa, the ratio between the modeled and observed
 423 fluxes can be close to one.

424 In addition to the IMF and solar wind parameters, we present the statistical de-
 425 pendencies on the geomagnetic indices K_p and SYM-H which are also the driving pa-
 426 rameters for IMPTAM. Figure 7 presents the modeled and observed electron fluxes binned
 427 by MLT with 1 hour step and K_p -index with 4 steps when moving from one K_p -value
 428 to the next, and then averaged, together with the ratio between them and the distribu-
 429 tion of data counts within the observed range of MLT and K_p . Contrary to the IMF and
 430 solar wind parameters, many more datapoints need to be considered in our analysis, ex-
 431 cept of those with $K_p > 5$ as can be seen in Figure 7j. The similar pattern how the ob-
 432 served electron fluxes depend on the K_p -index along the geostationary orbit was previ-
 433 ously reported using LANL MPA data (Korth et al., 1999) and Polar HYDRA data (Friedel
 434 et al., 2001). It is rather similar to the one for V_{SW} (Figure 5) with the U-shaped peaks
 435 on the downside with fluxes increasing as K_p increases. The modeled fluxes exhibit two
 436 orders of magnitude difference at around midnight for K_p greater than 5 but these cor-
 437 respond to statistically less meaningful bins. They are close to the observed fluxes at 06-
 438 12 MLT with the ratio of one or less.

439 Figure 8 shows the modeled and observed electron fluxes binned by MLT with 1
 440 hour step and SYM-H index with 5 nT step, and then averaged, together with the ra-
 441 tio between them and the distribution of data counts within the observed range of MLT
 442 and SYM-H. According to Figure 8j, we take into account the datapoints with SYM-H
 443 below 50 nT and above -60 nT. The observed 40 keV fluxes (Figure 8a) exhibit a clear
 444 peak for negative SYM-H values located at 00-06 MLT. This peak is present for 75 keV
 445 (Figure 8b) and 150 keV (Figure 8c) electron fluxes with an order of magnitude smaller
 446 fluxes but similar MLT location. The modeled fluxes again show the shift towards mid-
 447 night and order of magnitude over-estimates at 18-24 MLT. The ratio is close to one at
 448 around 06-12 MLT.

449 5 Metrics for model performance

450 The quality of any model is determined by how well this model predicts the quan-
 451 tities being modeled as compared to the real data and how much it deviates from the
 452 observations. There are several metrics to assess the model's quality and many of them
 453 have been successfully applied to terrestrial weather forecast models (Murphy, 1993; Thorne
 454 & Stephenson, 2001; Jolliffe & Stephenson, 2012). With the intense development of space
 455 weather forecast models, similar metrics can be applied for them, too (e.g., Lopez et al.,
 456 2007; Welling & Ridley, 2010; Pulkkinen et al., 2013; Ganushkina et al., 2015; Morley,
 457 2016; Morley et al., 2018).

458 Before computing the necessary metrics, in Figure 9, we present the scatter plots
 459 of GOES MAGED electron fluxes vs. fluxes by IMPTAM for (a) 50, (b) 75, and (c) 150
 460 keV. We overplot the fluxes with the scatter density which converts the population den-
 461 sity of the data into a logarithmic gradient. This logarithmic gradient of the points is
 462 denoted by the colorbar in these plots. As expected, there is no obvious one-to-one cor-
 463 relation. The observed dropouts (lowest fluxes for all three energies) are not reproduced
 464 (modeled fluxes stay high). It is also seen that there are times of low modeled fluxes that
 465 are not observed. These are dropouts from magnetopause shadowing in the model that

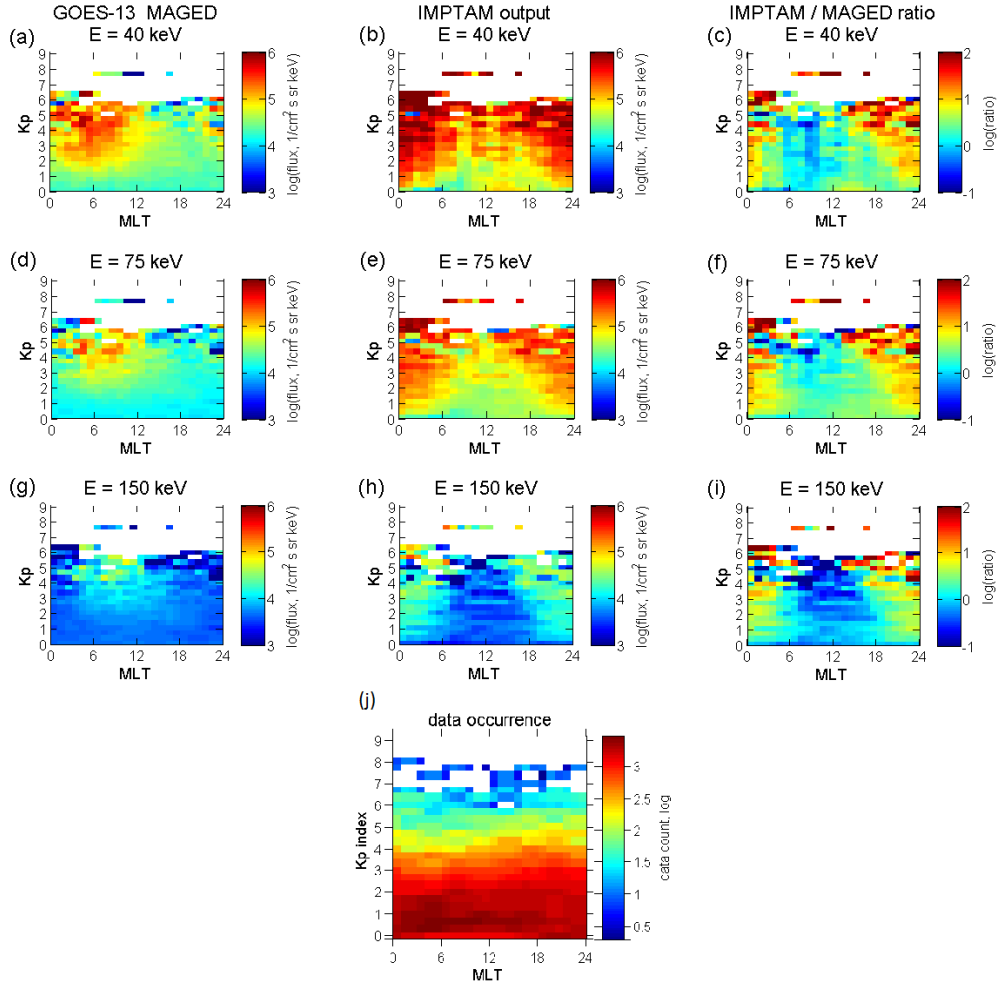


Figure 7. Similar to Figure 2 but the observed and modeled electron fluxes are binned by MLT and Kp-index and then averaged with Kp data occurrence.

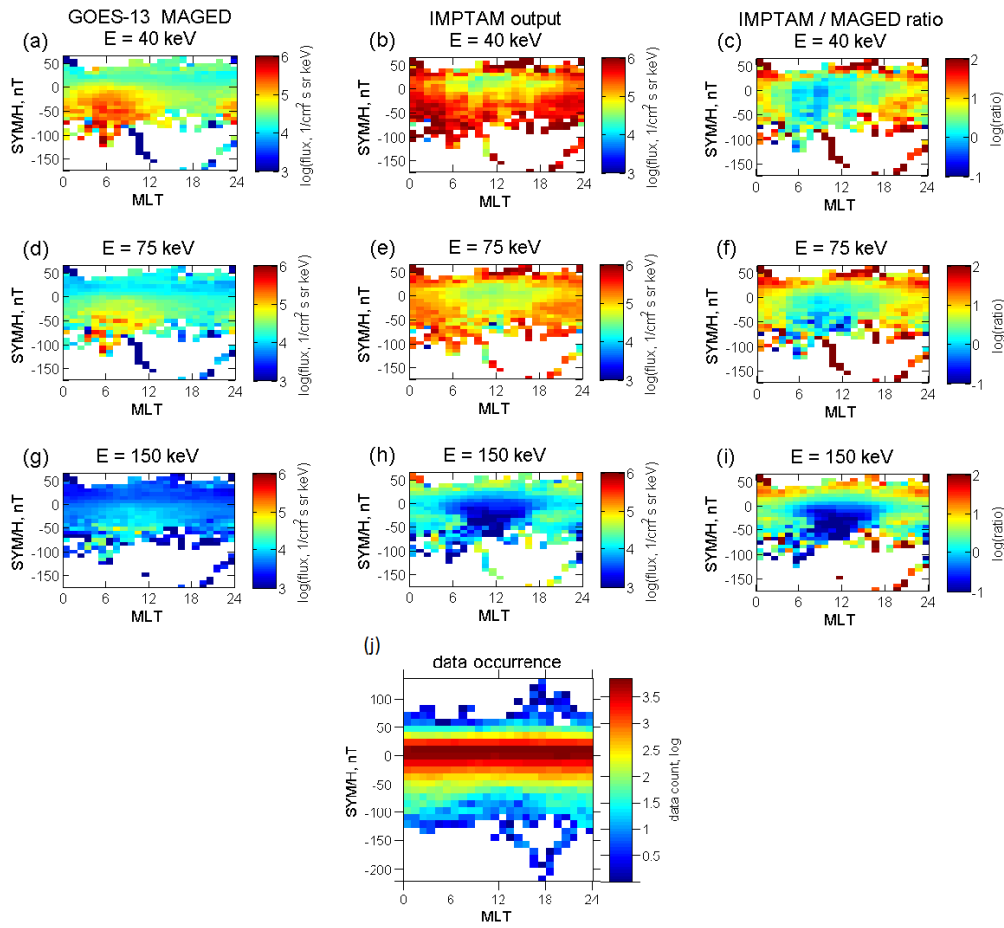


Figure 8. Similar to Figure 2 but the observed and modeled electron fluxes are binned by MLT and SYM-H index and then averaged with SYM-H data occurrence.

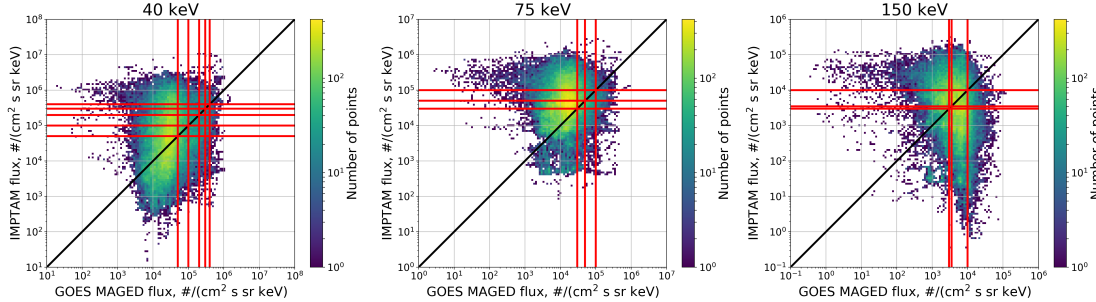


Figure 9. Scatter plots of GOES MAGED electron fluxes vs. modeled fluxes by IMPTAM for (a) 50, (b) 75, and (c) 150 keV overplotted with population density of the data, together with thresholds used for binary event analysis marked by red lines.

were not seen at GOES. Despite these "wings" of the distribution, there is a large cloud of points within an order of magnitude along the one-to-one black diagonal line.

To evaluate the quality of the electron flux forecasts made by the IMPTAM, we employ the binary event analysis (Jolliffe & Stephenson, 2012). This methodology first divides the time series data into non-overlapping time windows. Each interval is then categorized by the behavior of the model and observation with respect to a given threshold: it is considered a "Hit" if the model and data both cross the threshold, a "Miss" if the observation does but the model does not, a "False Positive" of the model does but the data does not, and a "True Negative" if neither cross. The thresholds for each energy level are given in the first column of Table 1 and Figure 9 shows them as red lines over the scatter plots. Ideally, these thresholds need to be meaningful for applications based on the fact that the surface charging can begin when electron fluxes exceed the threshold level which is spacecraft and energy dependent. Since we do not know them for GOES MAGED data, the selection of threshold levels is somewhat arbitrary. Any particular percentile of the observed flux is no more meaningful, either, since the surface potential on a satellite is not determined by a specific percentile. Therefore, in the present study we select several thresholds so that binary event metrics have enough events (i.e., threshold crossings) to be useful and the thresholds correspond to our previous analysis (Ganushkina et al., 2015) to be able to compare the results.

Following the our previous work (Ganushkina et al., 2015), the window width is set to one hour. One hour is rather long as compared to the model output every 5 minutes, the flux can vary significantly within an hour, but in the present study, the selected window is chosen to test "bulk activity". Columns 2-5 in Table 1 contain the actual numbers of Hits, False Positives, Misses and True Negatives. Descriptive metrics and skill scores can be calculated from them. One metric is the "Hit Rate", or the ratio of correctly predicted threshold crossings to all observed crossings. It ranges from 0 to 1, with 1 being perfect. Next is "False Alarm Rate", or the fraction of false alarms to all non-event intervals. Here, 0 is perfect and 1 indicates the model predicts a crossing at all times. Finally, we list the "Heidke Skill Score", which is the fraction of correct predictions when adjusted for those expected from pure random chance, is calculated. This value has the range [-1,1] where 1 is perfect and zero corresponds to a performance that is indistinguishable from random chance. The results for this analysis are shown in Table 1. In general, the model has an appreciable hit rate (20-78% of threshold crossings are reproduced depending on energy and threshold, see Table 1) for all energy levels and all thresholds. However, this is offset by considerable false alarm rates (crossings were incorrectly predicted during 14% to 50% of non-event times, see Table 1), which keep the Heidke skill scores modest at best. For 40 keV electrons, the model correctly forecasts 6 to 16% more

Table 1. Binary event analysis results for each energy channel as a function of flux threshold

Threshold, $cm^{-2} sec^{-1} sr^{-1} keV^{-1}$	Hit	False Positive	Miss	True Negative	Hit Rate	False Alarm Rate	Heidke Skill Score
40 keV electron fluxes							
$5 \cdot 10^4$	2051	3458	868	3419	0.703	0.503	0.159
$1 \cdot 10^5$	801	3217	553	5225	0.592	0.381	0.115
$2 \cdot 10^5$	346	2154	344	6952	0.501	0.237	0.120
$3 \cdot 10^5$	180	1702	197	7717	0.477	0.181	0.102
$4 \cdot 10^5$	84	1403	128	8181	0.396	0.146	0.063
75 keV electron fluxes							
$3 \cdot 10^4$	1707	5048	473	2598	0.783	0.660	0.070
$5 \cdot 10^4$	634	4303	394	4495	0.617	0.489	0.048
$1 \cdot 10^5$	154	2753	226	6693	0.405	0.291	0.027
150 keV electron fluxes							
$3 \cdot 10^3$	3717	1790	2931	730	0.559	0.710	-0.133
$3.5 \cdot 10^3$	3112	2062	2996	998	0.509	0.674	-0.153
$1 \cdot 10^4$	299	2561	1125	5183	0.210	0.331	-0.086

events than what is expected from a random forecast (and a bit lower values, 3-7%, for 75 keV). For 150 keV electrons, the performance is worse than a random forecast as the numbers are negative. In summary, the model is performing best at the 40 keV channel and for lower thresholds. It struggles at the 150 keV channel. The scores are in line with those reported in Ganushkina et al. (2015), with improvements found in the 40 keV channel predictions.

The IMPTAM performance level presented above is rather expected, since in case of electron fluxes observed by GOES MAGED, there are several orders of magnitude differences between the fluxes at different locations along geostationary orbit and during quiet and disturbed conditions with different levels of variability. For this reason, for example, using the scale-dependent accuracy measures such as simple model error or mean error can be problematic, since it can result in very large values due to the outliers in the data and in the model. Outliers influence the model performance significantly more than small deviations from the observations (Morley et al., 2018). Morley et al. (2018) presented a very thorough analysis of other descriptive metrics which can help better to illustrate the performance of the model. In our study, we follow the Morley et al. (2018) findings.

The first metric used here is the well-known Pearson correlation coefficient, a measure of linear correlation between the observations and model results. Next is “Median Symmetric Accuracy” (designated as ζ) expressed as

$$\zeta = 100(\exp(M(|\log_e(Q_i)|)) - 1), \quad (3)$$

where $Q_i = \frac{y_i}{x_i}$ is the accuracy ratio, which is the ratio between the modeled y_i and the observed x_i fluxes. As was shown in Tofallis (2015), $\log_e(Q)$ is best for the data with the variance depending on the magnitude of the variable which is the case for radiation belt electron fluxes and where this metric has been previously used (e.g., Morley, 2016; Reeves et al., 2011). Absolute values of $\log_e(Q)$ makes sure that the metric is symmetric (when the values of the modeled and observed fluxes are switched, the error is the same). The median function M and then exponent is used to return to the original units and scale.

531 One is subtracted so that the metric is in the $[0, \infty)$ range, multiplying by 100 gives the
 532 equivalent percentage error. Median symmetric accuracy can be interpreted as the me-
 533 dian percentage error. For example, if $\zeta = 50\%$, the model is most frequently report-
 534 ing values that are 50% larger or smaller than the observation at any given point.

535 The final metric used here is Symmetric Signed Percentage Bias (*SSPB*). The bias
 536 describes the difference between the average model output and the average observation.
 537 A negative bias indicates a systematic under-prediction, whereas a positive bias indicates
 538 a systematic over-prediction. Morley et al. (2018) presented a new measure of bias based
 539 on the log accuracy ratio

$$540 \quad SSPB = 100 \operatorname{sgn}(M(\log_e(Q_i)))(\exp(|M(\log_e(Q_i))|) - 1). \quad (4)$$

541 The magnitude of the bias is estimated by taking the absolute value of $M(\log_e(Q_i))$, one
 542 is subtracted so that the lower limit is zero, the direction of the bias is found using the
 543 signum function, and the metric is multiplied by 100 to express it as a percentage. This
 544 value reports the median bias of the model as a percentage of the observed value. For
 545 example, if $SSPB = -50\%$, the model is biased towards underprediction, most frequently
 546 reporting values that are 50% less than the corresponding observations. Both ζ and $SSPB$
 547 are defined in detail by Morley et al. (2018). While other measures of bias and accuracy
 548 exist, these are robust to data that spans orders of magnitude, as is the case with inner
 549 magnetosphere electron fluxes.

550 The correlation, accuracy, and bias metrics for the IMPTAM dataset compared to
 551 GOES 13 are shown in Table 2. Overall correlation is weak and appears inversely pro-
 552 portional to electron energy. ζ values demonstrate that the predictions are typically off
 553 by 200% (of almost 300% for 150 keV electrons). *SSPB* shows that the direction of the
 554 error varies with energy. Considered together with the binary event analysis, performance
 555 is best at the 40 keV level.

Table 2. Descriptive metrics for each energy channel.

	Energy Channel		
	40keV	75keV	150keV
Corr. Coeff	0.1300	0.0390	-0.1227
Accuracy (ζ)	232.75%	244.36%	292.40%
Bias (<i>SSPB</i>)	049.04%	189.34%	-17.86%

556 6 Discussion and Conclusions

557 We presented the validation study of the performance of the model for electrons
 558 with energies of 1 to few hundreds of keVs (IMPTAM) at geostationary orbit. keV elec-
 559 trons are important constituents of the near-Earth's radiation environment being the seed
 560 population for further acceleration to MeV energies in the radiation belts and posing a
 561 serious risk of surface charging for satellites. The 18.5 months of IMPTAM output taken
 562 from its continuous operation online in real time was compared to the corresponding data
 563 from the GOES 13 MAGED instrument for the flight direction integrated differential fluxes
 564 for energies of 40, 75, and 150 keV. In addition to the direct data-model comparison dur-
 565 ing the entire modeled period (as was done in Ganushkina et al. (2015)), the observed
 566 and modeled electron fluxes were organized by MLT along the GOES 13 orbit and the
 567 solar wind and IMF parameters and geomagnetic indices (IMF B_Z , B_Y components and
 568 strength $|B|$, V_{SW} and P_{SW} , K_p and SYM-H) which are the driving parameters for IMP-
 569 TAM and then compared. This approach provided more insights into the influence of
 570 the different parameters on the IMPTAM performance quality.

All the statistical patterns for all three energies binned by MLT and IMPTAM driving parameters have their peaks in electron fluxes at the dawnside as would be expected from the motion of electrons in the inner magnetosphere but the peaks for modeled fluxes are located not at around 06 MLT as for the observed fluxes but shifted towards midnight being between 00 and 06 MLT. This does not mean that the electrons in IMPTAM do not drift downward (the ratio between the observed and modeled fluxes at around 06 MLT is very close to one). This indicates that the modeled flux at around midnight is too high. There are several possible reasons for this. One of them is the representation of electron losses by introducing electron lifetimes as a combination of M. W. Chen et al. (2005) and Shprits et al. (2007) electron lifetimes for strong and weak diffusion, respectively. The Shprits et al. (2007) representation does not include the MLT-dependence but it has the Kp-dependence which is important when we apply these electron lifetimes at distances inside geostationary orbit. There is no dependence on geomagnetic activity in the M. W. Chen et al. (2005) representation but the MLT-dependence is present (although rather homogeneous and weak as can be seen in Figure 5 of M. W. Chen et al. (2005)) and it can be applied when we model electron motion from the plasma sheet to geostationary orbit. The model for electron lifetimes used in the present paper lacks the realistic distribution of waves as compared to, for example, the model of electron lifetimes due to interactions with chorus waves by Orlova and Shprits (2014) and with hiss waves by Orlova et al. (2016). These models are now incorporated into the new version of IMPTAM. For the 18.5 months of IMPTAM run, we used what was available at that time and the run was done without any changes.

Another reason for the excessive amount of electrons around midnight is the symmetry in the models used inside IMPTAM. For the electric field model, we used the Boyle et al. (1997) polar cap potential dependent on IMF and solar wind parameters but applied this to a Volland-Stern type two-cell convection pattern. Our choice was based on the need for dependence on IMF and solar wind parameters yet keeping it a rather simple model. There exist numerous models which can be used for the global convection electric field in the magnetosphere. In reality, particle transport from the plasma sheet does not occur in the Boyle-type potential. There are studies on penetration electric field (e.g., Ridley & Liemohn, 2002; Liemohn et al., 2004), concentrations of potential in narrow channels resulting in a fast transport of plasma sheet particles to the inner magnetosphere (M. W. Chen et al., 2003), existence of an extra potential well near local midnight (Fok et al., 2001, 2003). Usage of a simple representation for the electric field contributes to the presence of higher than observed fluxes at midnight. We are now in the process of testing the Weimer (2005) electric field model incorporated into IMPTAM which depends on the IMF clock angle, IMF total field and components, V_{SW} , P_{SW} , and AL index. For magnetic field, several of the latest models, such as the TA15 (Tsyganenko & Andreeva, 2015) model and the RBF (Radial Basis Function) model (Andreeva & Tsyganenko, 2016; Tsyganenko & Andreeva, 2016) are now being considered.

The third reason is related to using the Tsyganenko and Mukai (2003) model for boundary conditions at $10 R_E$ in the plasma sheet. Limitations of Tsyganenko and Mukai (2003) applied for electrons are discussed in Dubyagin et al. (2016). The modeled fluxes are affected by the model's parameterization for plasma sheet density and temperature and its simple $\sin^2(MLT)$ dependence. Dawn-dusk asymmetric terms are not included which sets the maximum location of density and temperature at around midnight. As for model parameters, for example, there will be an influx of electrons during both negative and positive IMF B_Z , and for positive IMF B_Z , the dependence is still proportional to the absolute value of B_Z . The distribution at the boundary fitted by the kappa shape with parameters as the electron number density and temperature in the plasma sheet which were obtained at distances between 6 and $11 R_E$ based on THEMIS data was given in Dubyagin et al. (2016) empirical model, usage of it will improve critically the IMPTAM outputs.

624 It needs to be mentioned that the version of IMPTAM used in the present paper
 625 did not include the effects from the substorm-associated electromagnetic fields. Substorms
 626 are a crucial factor in the transport and acceleration of keV electrons. Many satellite anomalies
 627 due to surface charging at geostationary orbit occur at night and early dawn (e.g.,
 628 Fennell et al., 2001; O'Brien, 2009) where a hot plasma is injected from the magneto-
 629 tail during substorms. Ganushkina et al. (2013, 2014), when modeling specific storm events,
 630 launched electromagnetic pulses given by Sarris et al. (2002) at each substorm onset de-
 631 termined from the AE index and scaled the amplitude according to the maximum val-
 632 ues of the AE index. Addition of effects from substorms can influence the long-term IMP-
 633 TAM performance.

634 All the statistical patterns for all three energies binned by MLT and IMPTAM driv-
 635 ing parameters exhibit very similar shapes for the observed and modeled fluxes. The dif-
 636 ferences of one to two orders of magnitude are present, though. At the same time, the
 637 largest differences are mainly seen for such ranges of driving parameters when the num-
 638 ber of datapoints (observed and modeled fluxes) is much less than 10% from the max-
 639 imum number of points in a bin in that MLT range. For example, unrealistically high
 640 modeled fluxes were obtained at large (> 10 nT) positive IMF B_Z at around 18-06 MLT.
 641 If during our analysis we concentrate only at the ranges of IMPTAM driving parame-
 642 ters where the number of datapoints is statistically significant and disregard those which
 643 constitute less than 10%, the average difference will be about one order of magnitude.
 644 At the same time, as was mentioned above, the ratio between the observed and mod-
 645 eled fluxes at around 06 MLT is very close to one.

646 (Sillanp et al., 2017) conducted the analysis of GOES 13 MAGED data for five years
 647 (2011-2015) and developed an empirical model for the electron fluxes at geostationary
 648 orbit. They found that IMF B_z and solar wind speed V_{SW} with time delay of 1.5 hours
 649 were the parameters that produced the best correlation between the modeled and ob-
 650 served electron fluxes, so the model used those two driving parameters. Both parame-
 651 ters are the driving parameters in IMPTAM. The ratio between the modeled and the ob-
 652 served fluxes at 00-12 MLT is close to one (with upper value of up to 10) for IMF B_Z
 653 range of -10 to 10 nT which has most of the datapoints (Figure 2). The same is true for
 654 modeled fluxes corresponding to $V_{SW} < 700$ km/s: main over-estimation of about one
 655 order of magnitude is seen at around midnight (Figure 5). This reasonable agreement
 656 between the MAGED and IMPTAM fluxes is a valuable achievement for IMPTAM val-
 657 idation.

658 To evaluate the quality of the electron flux forecasts made by the IMPTAM, we
 659 employed the binary event analysis. The window width was set to one hour which is rather
 660 long, since the flux can vary significantly within an hour, but in the present study, the
 661 selected window is chosen to test “bulk activity”. It was found that, in general, IMP-
 662 TAM performs with the hit rate of 20-78% of threshold crossings reproduced depend-
 663 ing on energy and threshold, see Table 1). The Heidke skill scores are rather low (0.159
 664 at best for 40 keV electrons and negative values (-0.133) for 150 keV electrons) due to
 665 considerable false alarm rates (incorrect predictions during 14% to 50% of non-event times).
 666 The model is best at the 40 keV channel and for lower thresholds. This is very similar
 667 to that what was found in the previous study (Ganushkina et al., 2015), although some
 668 improvements are present for the 40 keV electrons. Three more metrics, namely, corre-
 669 lation, accuracy, and bias metrics, were used for the IMPTAM output compared to GOES
 670 13 data. Overall correlation is rather weak and appears inversely proportional to elec-
 671 tron energy. Median Symmetric Accuracy values demonstrate that the modeled fluxes
 672 are off by a factor of two (up to 3 for 150 keV electrons). Symmetric Signed Percentage
 673 Bias shows that the direction of the error varies with energy: the model overpredicts by
 674 50% for 40 keV, underpredicts by 18% for 150 keV and overpredicts by almost 200% for
 675 75 keV electrons. As was mentioned in Section 5, it is hard to expect the perfect per-
 676 formance of IMPTAM due to variations of several orders of magnitudes seen in keV elec-

tron fluxes which are strongly dependent on location and geomagnetic conditions. The main factors influencing the IMPTAM performance, especially at 150 keV, are the (1) boundary conditions were developed for ions but used here for electrons, (2) absence of substorm effects, (3) representations of electric and magnetic fields which can result in not enough adiabatic acceleration, and (4) effects from wave-particle interactions introduced as simple electron lifetimes. Ongoing work for IMPTAM improvement takes into account these factors. The Heidke skill scores are also influenced by the somewhat arbitrary selection of the thresholds for its calculation and the window width. The analysis conducted here provides insights into the representation of physical processes inside the IMPTAM. Special attention should be paid to these issues when improving IMPTAM in the future.

It needs to be stressed here that the analysis presented is for “nowcast” IMPTAM output, which is in contrast to “pastcast” when finalized, not real time driving parameters can be used and the IMPTAM setup can be varied to achieve the best fit to the data. The present study analyzes the IMPTAM output when it was run online in real time continuously, without introducing any changes into its structure and with the driving parameters always taken as real time parameters. It was a specific intention to present the IMPTAM performance on a sufficiently long time period without any interventions into its operation and without any “pastcast”-type approach.

Keeping in mind the points discussed above, the conclusions are the following:

1. The peaks for IMPTAM modeled fluxes are located not at around 06 MLT as for the observed GOES 13 MAGED fluxes but shifted towards midnight at all statistical patterns binned by MLT and IMPTAM driving parameters for all three energies.

2. All the statistical patterns for all three energies binned by MLT and IMPTAM driving parameters exhibit very similar features for the observed and modeled fluxes with the largest differences of about one order of magnitude. Differences of two orders of magnitude are seen for all IMPTAM parameters when the number of datapoints is less than 10% from the maximum number per bin. At the same time, the ratio between the observed and modeled fluxes at around 06 MLT is very close to one.

3. The IMF B_z and solar wind speed V_{SW} are the parameters which organize best the observed and modeled electron fluxes.

4. The applied metrics demonstrate that (a) in binary event analysis, 20-78% of threshold crossings are reproduced depending on energy and threshold but Heidke skill scores are not higher than 0.159 for 40 keV electrons and negative for 150 keV electrons due to incorrect predictions during 14% to 50% of non-event times; (b) the correlations are weak; (c) modeled fluxes are off by 200% (and up to 300% for 150 keV electrons) in terms of the median symmetric accuracy; and (d) symmetric signed percentagebias shows that the direction of the error varies with energy: overprediction by 50% (40 keV), overprediction by 200% (75 keV), underprediction by 18% (150 keV). Performance is best at the 40 keV level.

5. The revealed discrepancies are due to the models inside IMPTAM, such as (1) boundary conditions developed for ions but used for electrons, (2) absence of substorm effects, (3) representations of electric and magnetic fields which can result in not enough adiabatic acceleration, and (4) effects from wave-particle interactions introduced as simple electron lifetimes.

There is a further need to evaluate the model performance on larger data sets and with more appropriate metrics. The models like IMPTAM provide the information about the radiation environment which is vital and necessary to have in order to estimate the surface charging effects on satellites. When an anomaly occurs, the radiation environment may be more extreme than that given by the specification models used for design.

727 The existence of an operational model, fully validated and run in real time, is extremely
 728 important for determining the possible reason for that anomaly.

729 **Acknowledgments**

730 The projects leading to these results have received funding from the European Union
 731 Seventh Framework Programme (FP7/2007-2013) under grant agreement No 606716 SPACES-
 732 TORM and from the European Union's Horizon 2020 research and innovation program
 733 under grant agreement No 637302 PROGRESS. N. Ganushkina thanks the International
 734 Space Science Institute in Bern, Switzerland, for their support of the international teams
 735 on "Analysis of Cluster Inner Magnetosphere Campaign data, in application of the dy-
 736 namics of waves and wave-particle interaction within the outer radiation belt" and "Ring
 737 current modeling: Uncommon Assumptions and Common Misconceptions". The con-
 738 tribution by S. Dubyagin has been supported by the framework of the Finnish Centre
 739 of Excellence in Research of Sustainable Space (Academy of Finland decision numbers
 740 312351 and 312390), which we gratefully acknowledge. The work at the University of Michi-
 741 gan was partly supported by the National Aeronautics and Space Administration un-
 742 der grant agreement NNX17AI48G and by the National Science Foundation under grant
 743 agreement NSF 1663770. The work at the University of Colorado was supported by the
 744 National Centers for Environmental Information under cooperative agreement NA17OAR4320101.

745 The IMPTAM output can be found at <https://umich.box.com/s/axce0pxezdrudkwldfn5r6vvg92zylzz>.

746 **References**

747 Andreeva, V. A., & Tsyganenko, N. A. (2016). Reconstructing the magnetosphere
 748 from data using radial basis functions. *Journal of Geophysical Research: Space
 749 Physics*, 121(3), 2249-2263. doi: 10.1002/2015JA022242

750 Baker, D., Erickson, P. J., Fennell, J. F., Foster, J. C., Jaynes, A. N., & Verronen,
 751 P. T. (2018). Space Weather Effects in the Earths Radiation Belts. *Space
 752 Science Reviews*, 214, 17. doi: 10.1007/s11214-017-0452-7

753 Balch, C. C. (2008). Updated verification of the Space Weather Prediction Center's
 754 solar energetic particle prediction model. *Space Weather*, 6(1). doi: 10.1029/
 755 2007SW000337

756 Balikhin, M. A., Boynton, R. J., Walker, S. N., Borovsky, J. E., Billings, S. A., &
 757 Wei, H. L. (2011). Using the NARMAX approach to model the evolution of
 758 energetic electrons fluxes at geostationary orbit. *Geophysical Research Letters*,
 759 38(18). doi: 10.1029/2011GL048980

760 Balikhin, M. A., Rodriguez, J. V., Boynton, R. J., Walker, S. N., Aryan, H., Sibeck,
 761 D. G., & Billings, S. A. (2016). Comparative analysis of NOAA REFM and
 762 SNB3GEO tools for the forecast of the fluxes of highenergy electrons at GEO.
 763 *Space Weather*, 14, 22-31. doi: 10.1002/2015SW001303

764 Boyd, A. J., Spence, H. E., Huang, C.-L., Reeves, G. D., Baker, D. N., Turner,
 765 D. L., ... Shprits, Y. Y. (2016). Statistical properties of the radiation belt
 766 seed population. *Journal of Geophysical Research: Space Physics*, 121(8),
 767 7636-7646. doi: 10.1002/2016JA022652

768 Boyle, C. B., Reiff, P. H., & Hairston, M. R. (1997). Empirical polar cap poten-
 769 tials. *Journal of Geophysical Research: Space Physics*, 102(A1), 111-125. doi:
 770 10.1029/96JA01742

771 Boynton, R. J., Balikhin, M. A., Sibeck, D. G., Walker, S. N., Billings, S. A., &
 772 Ganushkina, N. (2016). Electron flux models for different energies at geosta-
 773 tionary orbit. *Space Weather*, 14(10), 846-860. doi: 10.1002/2016SW001506

774 Brautigam, D. H., & Albert, J. M. (2000). Radial diffusion analysis of outer ra-
 775 diation belt electrons during the October 9, 1990, magnetic storm. *Jour-
 776 nal of Geophysical Research: Space Physics*, 105(A1), 291-309. doi:

777 10.1029/1999JA900344

778 Chen, M. W., Schulz, M., Anderson, P. C., Lu, G., Germany, G., & West, M.
 779 (2005). Storm time distributions of diffuse auroral electron energy and X-
 780 ray flux: Comparison of drift-loss simulations with observations. *Journal of*
 781 *Geophysical Research: Space Physics*, 110(A3). doi: 10.1029/2004JA010725

782 Chen, M. W., Schulz, M., Lu, G., & Lyons, L. R. (2003). Quasi-steady drift paths in
 783 a model magnetosphere with AMIE electric field: Implications for ring current
 784 formation. *Journal of Geophysical Research: Space Physics*, 108(A5). doi:
 785 10.1029/2002JA009584

786 Chen, Y., Friedel, R. H. W., & Reeves, G. D. (2006). Phase space density distribu-
 787 tions of energetic electrons in the outer radiation belt during two Geospace En-
 788 vironment Modeling Inner Magnetosphere/Storms selected storms. *Journal of*
 789 *Geophysical Research: Space Physics*, 111(A11). doi: 10.1029/2006JA011703

790 Chen, Y., Reeves, G. D., & Friedel, R. H. W. (2007). The energization of relativis-
 791 tic electrons in the outer Van Allen radiation belt. *Nature Physics*, 3, 614-617.
 792 doi: 10.1038/nphys655

793 Davis, V. A., Mandell, M. J., & Thomsen, M. F. (2008). Representation of the
 794 measured geosynchronous plasma environment in spacecraft charging calcu-
 795 lations. *Journal of Geophysical Research: Space Physics*, 113(A10). doi:
 796 10.1029/2008JA013116

797 Denton, M. H., Henderson, M. G., Jordanova, V. K., Thomsen, M. F., Borovsky,
 798 J. E., Woodroffe, J., ... Pitchford, D. (2016). An improved empirical model of
 799 electron and ion fluxes at geosynchronous orbit based on upstream solar wind
 800 conditions. *Space Weather*, 14(7), 511-523. doi: 10.1002/2016SW001409

801 Denton, M. H., Reeves, G. D., Larsen, B. A., Friedel, R. H. W., Thomsen, M. F.,
 802 Fernandes, P. A., ... Sarno-Smith, L. K. (2017). On the origin of low-energy
 803 electrons in the inner magnetosphere: Fluxes and pitch-angle distributions.
 804 *Journal of Geophysical Research: Space Physics*, 122(2), 1789-1802. doi:
 805 10.1002/2016JA023648

806 Denton, M. H., Thomsen, M. F., Jordanova, V. K., Henderson, M. G., Borovsky,
 807 J. E., Denton, J. S., ... Hartley, D. P. (2015). An empirical model of elec-
 808 tron and ion fluxes derived from observations at geosynchronous orbit. *Space*
 809 *Weather*, 13(4), 233-249. doi: 10.1002/2015SW001168

810 Doswell III, C. A., Davies-Jones, R., & Keller, D. L. (1990). On summary
 811 measures of skill in rare event forecasting based on contingency tables.
 812 *Weather Forecasting*, 5, 576-585. doi: 10.1175/1520-0434(1990)005<0576:
 813 OSMOSI>2.0.CO;2

814 Dubyagin, S., Ganushkina, N. Y., Sillanp, I., & Runov, A. (2016). Solar wind-driven
 815 variations of electron plasma sheet densities and temperatures beyond geo-
 816 stationary orbit during storm times. *Journal of Geophysical Research: Space*
 817 *Physics*, 121(9), 8343-8360. doi: 10.1002/2016JA022947

818 Fennell, J. F., Koons, H. C., Roeder, J. L., & Blake, J. B. (2001). *Spacecraft Charg-
 819 ing: Observations and Relationship to Satellite Anomalies* (Vol. 476). European
 820 Space Agency, Noordwijk, Netherlands.

821 Fok, M.-C., Buzulukova, N. Y., Chen, S.-H., Glocer, A., Nagai, T., Valek, P., &
 822 Perez, J. D. (2014). The Comprehensive Inner Magnetosphere-Ionosphere
 823 Model. *Journal of Geophysical Research: Space Physics*, 119(9), 7522-7540.
 824 doi: 10.1002/2014JA020239

825 Fok, M.-C., Glocer, A., Zheng, Q., Horne, R. B., Meredith, N. P., Albert, J. M., &
 826 Nagai, T. (2011). Recent developments in the radiation belt environment
 827 model. *Journal of Atmospheric and Solar-Terrestrial Physics*, 73(11), 1435-
 828 1443. doi: <https://doi.org/10.1016/j.jastp.2010.09.033>

829 Fok, M.-C., & Moore, T. E. (1997). Ring current modeling in a realistic magnetic
 830 field configuration. *Geophysical Research Letters*, 24(14), 1775-1778. doi: 10
 831 .1029/97GL01255

832 Fok, M.-C., Moore, T. E., & Delcourt, D. C. (1999). Modeling of inner plasma sheet
 833 and ring current during substorms. *Journal of Geophysical Research: Space*
 834 *Physics*, 104(A7), 14557-14569. doi: 10.1029/1999JA900014

835 Fok, M.-C., Moore, T. E., Wilson, G. R., Perez, J. D., Zhang, X. X., Brandt, P. C.,
 836 ... Wolf, R. A. (2003). Global ENA Image Simulations. *Space Science Re-*
 837 *views*, 109(1), 77-103. doi: 10.1023/B:SPAC.0000007514.56380.fd

838 Fok, M.-C., Wolf, R. A., Spiro, R. W., & Moore, T. E. (2001). Comprehensive
 839 computational model of Earth's ring current. *Journal of Geophysical Research: Space*
 840 *Physics*, 106(A5), 8417-8424. doi: 10.1029/2000JA000235

841 Foster, J. C., Erickson, P. J., Omura, Y., Baker, D. N., Kletzing, C. A., & Claude-
 842 pierre, S. G. (2017). Van Allen Probes observations of prompt mev ra-
 843 diation belt electron acceleration in nonlinear interactions with VLF cho-
 844 rus. *Journal of Geophysical Research: Space Physics*, 122(1), 324-339. doi:
 845 10.1002/2016JA023429

846 Friedel, R. H. W., Korth, H., Henderson, M. G., Thomsen, M. F., & Scudder,
 847 J. D. (2001). Plasma sheet access to the inner magnetosphere. *Journal*
 848 *of Geophysical Research: Space Physics*, 106(A4), 5845-5858. doi:
 849 10.1029/2000JA003011

850 Ganushkina, N. Y., Amariutei, O. A., Shprits, Y. Y., & Liemohn, M. W. (2013).
 851 Transport of the plasma sheet electrons to the geostationary distances.
 852 *Journal of Geophysical Research: Space Physics*, 118(1), 82-98. doi:
 853 10.1029/2012JA017923

854 Ganushkina, N. Y., Amariutei, O. A., Welling, D., & Heynderickx, D. (2015).
 855 Nowcast model for low-energy electrons in the inner magnetosphere. *Space*
 856 *Weather*, 13(1), 16-34. doi: 10.1002/2014SW001098

857 Ganushkina, N. Y., Liemohn, M. W., Amariutei, O. A., & Pitchford, D. (2014).
 858 Low-energy electrons (550 keV) in the inner magnetosphere. *Journal of*
 859 *Geophysical Research: Space Physics*, 119(1), 246-259. doi: 10.1002/
 860 2013JA019304

861 Garrett, H. B. (1981). The charging of spacecraft surfaces. *Reviews of Geophysics*,
 862 19(4), 577-616. doi: 10.1029/RG019i004p00577

863 Glauert, S. A., Horne, R. B., & Meredith, N. P. (2014). Three-dimensional elec-
 864 tron radiation belt simulations using the BAS Radiation Belt Model with
 865 new diffusion models for chorus, plasmaspheric hiss, and lightning-generated
 866 whistlers. *Journal of Geophysical Research: Space Physics*, 119(1), 268-289.
 867 doi: 10.1002/2013JA019281

868 Green, J. C., & Kivelson, M. G. (2001). A tale of two theories: How the adiabatic
 869 response and ulf waves affect relativistic electrons. *Journal of Geophysical Re-*
 870 *search: Space Physics*, 106(A11), 25777-25791. doi: 10.1029/2001JA000054

871 Green, J. C., & Kivelson, M. G. (2004). Relativistic electrons in the outer radiation
 872 belt: Differentiating between acceleration mechanisms. *Journal of Geophysical*
 873 *Research: Space Physics*, 109(A3). doi: 10.1029/2003JA010153

874 Hanser, F. A. (2011). *EPS/HEPAD calibration and data handbook* (Tech.
 875 Rep. GOESN-ENG-048D). Assurance Technology Corporation, Carlisle,
 876 Mass. Retrieved from <http://www.ngdc.noaa.gov/stp/satellite/goes/documentation.html>

878 Hartley, D. P., Denton, M. H., Green, J. C., Onsager, T. G., Rodriguez, J. V., &
 879 Singer, H. J. (2013). Case studies of the impact of high-speed solar wind
 880 streams on the electron radiation belt at geosynchronous orbit: Flux, magnetic
 881 field, and phase space density. *Journal of Geophysical Research: Space Physics*,
 882 118(11), 6964-6979. doi: 10.1002/2013JA018923

883 Heidke, P. (1926). Berechnung Des Erfolges Und Der Gte Der Windstrkevorher-
 884 sagen Im Sturmwarnungsdienst. *Geografiska AnnalerNature*, 8, 301-349. doi:
 885 10.1080/20014422.1926.11881138

886 Horne, R. B., Thorne, R. M., Shprits, Y. Y., Meredith, N. P., Glauert, S. A., Smith,

887 A. J., ... Decreau, P. M. E. (2005). Wave acceleration of electrons in the Van
 888 Allen radiation belts. *Nature*, *437*, 227-230. doi: doi:10.1038/nature03939

889 Iucci, N., Levitin, A. E., Belov, A. V., Eroshenko, E. A., Ptitsyna, N. G., Villoresi,
 890 G., ... G., Y. V. (2005). Space weather conditions and spacecraft anomalies in
 891 different orbits. *Space Weather*, *3*, S01001. doi: doi:10.1029/2003SW000056

892 Jaynes, A. N., Baker, D. N., Singer, H. J., Rodriguez, J. V., Loto'aniu, T. M., Ali,
 893 A. F., ... Reeves, G. D. (2015). Source and seed populations for relativistic
 894 electrons: Their roles in radiation belt changes. *Journal of Geophysical
 895 Research: Space Physics*, *120*(9), 7240-7254. doi: 10.1002/2015JA021234

896 Jolliffe, I. T., & Stephenson, D. B. (Eds.). (2012). *Forecast verification, A practi-
 897 tioner's guide in atmospheric science* (Second ed.). Wiley.

898 Jordanova, V. K., & Miyoshi, Y. (2005). Relativistic model of ring current and
 899 radiation belt ions and electrons: Initial results. *Geophysical Research Letters*,
 900 *32*(14). doi: 10.1029/2005GL023020

901 Jordanova, V. K., Yu, Y., Niehof, J. T., Skoug, R. M., Reeves, G. D., Kletzing,
 902 C. A., ... Spence, H. E. (2014). Simulations of inner magnetosphere dy-
 903 namics with an expanded RAM-SCB model and comparisons with Van Allen
 904 Probes observations. *Geophysical Research Letters*, *41*(8), 2687-2694. doi:
 905 10.1002/2014GL059533

906 Katus, R. M., & Liemohn, M. W. (2013). Similarities and differences in low- to
 907 middle-latitude geomagnetic indices. *Journal of Geophysical Research: Space
 908 Physics*, *118*(8), 5149-5156. doi: 10.1002/jgra.50501

909 Kennel, C. F., & Petschek, H. E. (1966). Limit on stably trapped particle fluxes.
 910 *Journal of Geophysical Research*, *71*(1), 1-28. doi: 10.1029/JZ071i001p00001

911 Kennel, C. F., & Thorne, R. M. (1967). Unstable growth of unducted whistlers
 912 propagating at an angle to the geomagnetic field. *Journal of Geophysical Re-
 913 search*, *72*(3), 871-878. doi: 10.1029/JZ072i003p00871

914 Kerns, K. J., Hardy, D. A., & Gussenhoven, M. S. (1994). Modeling of convection
 915 boundaries seen by CRRES in 120-eV to 28-keV particles. *Journal of Geophys-
 916 ical Research: Space Physics*, *99*(A2), 2403-2414. doi: 10.1029/93JA02767

917 Korth, H., Thomsen, M. F., Borovsky, J. E., & McComas, D. J. (1999). Plasma
 918 sheet access to geosynchronous orbit. *Journal of Geophysical Research: Space
 919 Physics*, *104*(A11), 25047-25061. doi: 10.1029/1999JA900292

920 Lanzerotti, L. J., LaFleur, K., MacLennan, C. G., & Maurer, D. W. (1998). Geosyn-
 921 chronous spacecraft charging in January 1997. *Geophysical Research Letters*,
 922 *25*(15), 2967-2970. doi: 10.1029/98GL00987

923 Leontaritis, I. J., & Billings, S. A. (1985a). Input-output parametric models for non-
 924 linear systems Part I: deterministic non-linear systems. *International Journal
 925 of Control*, *41*(2), 303-328. doi: 10.1080/0020718508961129

926 Leontaritis, I. J., & Billings, S. A. (1985b). Input-output parametric models for non-
 927 linear systems Part II: stochastic non-linear systems. *International Journal of
 928 Control*, *41*(2), 329-344. doi: 10.1080/0020718508961130

929 Li, W., Thorne, R. M., Ma, Q., Ni, B., Bortnik, J., Baker, D. N., ... Claudepierre,
 930 S. G. (2014). Radiation belt electron acceleration by chorus waves during the
 931 17 March 2013 storm. *Journal of Geophysical Research: Space Physics*, *119*(6),
 932 4681-4693. doi: 10.1002/2014JA019945

933 Liemohn, M. W., Khazanov, G. V., & Kozyra, J. U. (1998). Banded electron struc-
 934 ture formation in the inner magnetosphere. *Geophysical Research Letters*,
 935 *25*(6), 877-880. doi: 10.1029/98GL00411

936 Liemohn, M. W., Ridley, A. J., Gallagher, D. L., Ober, D. M., & Kozyra, J. U.
 937 (2004). Dependence of plasmaspheric morphology on the electric field descrip-
 938 tion during the recovery phase of the 17 April 2002 magnetic storm. *Journal of
 939 Geophysical Research: Space Physics*, *109*(A3). doi: 10.1029/2003JA010304

940 Lopez, R. E., Hernandez, S., Wiltberger, M., Huang, C.-L., Kepko, E. L., Spence,
 941 H., ... Lyon, J. G. (2007). Predicting magnetopause crossings at geosyn-

chronous orbit during the Halloween storms. *Space Weather*, 5(1). doi: 10.1029/2006SW000222

Mato-Vlez, J.-C., Sicard, A., Payan, D., Ganushkina, N., Meredith, N. P., & Sil-lanpa, I. (2018). Spacecraft surface charging induced by severe environments at geosynchronous orbit. *Space Weather*, 16(1), 89-106. doi: 10.1002/2017SW001689

Mauk, B. H., & Meng, C.-I. (1983). Characterization of geostationary particle signatures based on the “Injection Boundary” Model. *Journal of Geophysical Research: Space Physics*, 88(A4), 3055-3071. doi: 10.1029/JA088iA04p03055

Miyoshi, Y. S., Jordanova, V. K., Morioka, A., Thomsen, M. F., Reeves, G. D., Evans, D. S., & Green, J. C. (2006). Observations and modeling of energetic electron dynamics during the October 2001 storm. *Journal of Geophysical Research: Space Physics*, 111(A11). doi: 10.1029/2005JA011351

Morley, S. K. (2016). *Alternatives to accuracy and bias metrics based on percentage errors for radiation belt modeling applications* (Tech. Rep. LA-UR-16-24592). Los Alamos, NM 87545, USA: Los Alamos National Laboratory. doi: doi:10.2172/1260362

Morley, S. K., Brito, T. V., & Welling, D. T. (2018). Measures of Model Performance Based On the Log Accuracy Ratio. *Space Weather*, 16(1), 69-88. doi: 10.1002/2017SW001669

Murphy, A. H. (1993). What Is a Good Forecast? An Essay on the Nature of Goodness in Weather Forecasting. *Weather and Forecasting*, 8(2), 281-293. doi: 10.1175/1520-0434(1993)008<0281:WIAGFA>2.0.CO;2

O’Brien, T. P. (2009). SEAES-GEO: A spacecraft environmental anomalies expert system for geosynchronous orbit. *Space Weather*, 7(9). doi: 10.1029/2009SW000473

Orlova, K., & Shprits, Y. (2014). Model of lifetimes of the outer radiation belt electrons in a realistic magnetic field using realistic chorus wave parameters. *Journal of Geophysical Research: Space Physics*, 119(2), 770-780. doi: 10.1002/2013JA019596

Orlova, K., Shprits, Y., & Spasojevic, M. (2016). New global loss model of energetic and relativistic electrons based on Van Allen Probes measurements. *Journal of Geophysical Research: Space Physics*, 121(2), 1308-1314. doi: 10.1002/2015JA021878

Pulkkinen, A., Rasttter, L., Kuznetsova, M., Singer, H., Balch, C., Weimer, D., ... Weigel, R. (2013). Community-wide validation of geospace model ground magnetic field perturbation predictions to support model transition to operations. *Space Weather*, 11(6), 369-385. doi: 10.1002/swe.20056

Reeves, G. D., Morley, S. K., Friedel, R. H. W., Henderson, M. G., Cayton, T. E., Cunningham, G., ... Thomsen, D. (2011). On the relationship between relativistic electron flux and solar wind velocity: Paulikas and Blake revisited. *Journal of Geophysical Research: Space Physics*, 116(A2), A02213. doi: 10.1029/2010JA015735

Ridley, A. J., & Liemohn, M. W. (2002). A model-derived storm time asymmetric ring current driven electric field description. *Journal of Geophysical Research: Space Physics*, 107(A8), SMP 2-1-SMP 2-12. doi: 10.1029/2001JA000051

Roberts, C. S. (1965). On the relationship between the unidirectional and omnidirectional flux of trapped particles on a magnetic line of force. *Journal of Geophysical Research*, 70(11), 2517-2527. doi: 10.1029/JZ070i011p02517

Rodriguez, J. V. (2014). *GOES 13-15 MAGE/PD pitch angles* (Algorithm Theoretical Basis Document, version 1.0). NOAA NESDIS NGDC. Retrieved from <http://www.ngdc.noaa.gov/stp/satellite/goes/documentation.html>

Rowland, W., & Weigel, R. S. (2012). Intracalibration of particle detectors on a three-axis stabilized geostationary platform. *Space Weather*, 10(11). doi: 10.1029/2012SW000816

997 Sarris, T. E., Li, X., Tsaggas, N., & Paschalidis, N. (2002). Modeling energetic par-
 998 ticle injections in dynamic pulse fields with varying propagation speeds. *Journal*
 999 *of Geophysical Research: Space Physics*, 107(A3), SMP 1-1-SMP 1-10. doi:
 1000 10.1029/2001JA900166

1001 Schulz, M., & Lanzerotti, L. J. (1974). *Particle Diffusion in the Radiation Belts*
 1002 (Vol. 7). Springer-Verlag, New York.

1003 Shprits, Y. Y., Meredith, N. P., & Thorne, R. M. (2007). Parameterization of radi-
 1004 ation belt electron loss timescales due to interactions with chorus waves. *Geo-*
 1005 *physical Research Letters*, 34(11). doi: 10.1029/2006GL029050

1006 Shprits, Y. Y., Thorne, R. M., Horne, R. B., & Summers, D. (2006). Bounce-
 1007 averaged diffusion coefficients for field-aligned chorus waves. *Journal of Geo-*
 1008 *physical Research: Space Physics*, 111(A10). doi: 10.1029/2006JA011725

1009 Sillanp, I., Ganushkina, N. Y., Dubyagin, S., & Rodriguez, J. V. (2017). Electron
 1010 Fluxes at Geostationary Orbit From GOES MAGED Data. *Space Weather*,
 1011 15(12), 1602-1614. doi: 10.1002/2017SW001698

1012 Subbotin, D. A., & Shprits, Y. Y. (2009). Three-dimensional modeling of the ra-
 1013 diation belts using the Versatile Electron Radiation Belt (VERB) code. *Space*
 1014 *Weather*, 7(10). doi: 10.1029/2008SW000452

1015 Thomsen, M. F., Henderson, M. G., & Jordanova, V. K. (2013). Statistical prop-
 1016 erties of the surface-charging environment at geosynchronous orbit. *Space*
 1017 *Weather*, 11(5), 237-244. doi: 10.1002/swe.20049

1018 Thornes, J. E., & Stephenson, D. B. (2001). How to judge the quality and value of
 1019 weather forecast products. *Meteorological Applications*, 8(3), 307-314. doi: 10
 1020 .1017/S1350482701003061

1021 Tofallis, C. (2015). A better measure of relative prediction accuracy for model selec-
 1022 tion and model estimation. *Journal of the Operational Research Society*, 66(8),
 1023 1352-1362. doi: 10.1057/jors.2014.103

1024 Tsyganenko, N. A. (1995). Modeling the Earth's magnetospheric magnetic field con-
 1025 fined within a realistic magnetopause. *Journal of Geophysical Research: Space*
 1026 *Physics*, 100(A4), 5599-5612. doi: 10.1029/94JA03193

1027 Tsyganenko, N. A., & Andreeva, V. A. (2015). A forecasting model of the magneto-
 1028 sphere driven by an optimal solar wind coupling function. *Journal of Geophysi-
 1029 cal Research: Space Physics*, 120(10), 8401-8425. doi: 10.1002/2015JA021641

1030 Tsyganenko, N. A., & Andreeva, V. A. (2016). An empirical RBF model of the mag-
 1031 netosphere parameterized by interplanetary and ground-based drivers. *Journal*
 1032 *of Geophysical Research: Space Physics*, 121(11), 10,786-10,802. doi: 10.1002/
 1033 2016JA023217

1034 Tsyganenko, N. A., & Mukai, T. (2003). Tail plasma sheet models derived from Geo-
 1035 tail particle data. *Journal of Geophysical Research: Space Physics*, 108(A3).
 1036 doi: 10.1029/2002JA009707

1037 Usanova, M. E., Drozdov, A., Orlova, K., Mann, I. R., Shprits, Y., Robertson,
 1038 M. T., ... Wygant, J. (2014). Effect of EMIC waves on relativistic
 1039 and ultrarelativistic electron populations: Ground-based and Van Allen
 1040 Probes observations. *Geophysical Research Letters*, 41(5), 1375-1381. doi:
 1041 10.1002/2013GL059024

1042 Walther, B. A., & Moore, J. L. (2005). The concepts of bias, precision and accuracy,
 1043 and their use in testing the performance of species richness estimators, with a
 1044 literature review of estimator performance. *Ecography*, 28(6), 815-829. doi:
 1045 10.1111/j.2005.0906-7590.04112.x

1046 Wanliss, J. A., & Showalter, K. M. (2006). High-resolution global storm index: Dst
 1047 versus SYM-H. *Journal of Geophysical Research: Space Physics*, 111(A2). doi:
 1048 10.1029/2005JA011034

1049 Weimer, D. R. (2005). Improved ionospheric electrodynamic models and applica-
 1050 tion to calculating Joule heating rates. *Journal of Geophysical Research: Space*
 1051 *Physics*, 110(A5). doi: 10.1029/2004JA010884

1052 Welling, D. T., & Ridley, A. J. (2010). Validation of SWMF magnetic field and
1053 plasma. *Space Weather*, 8(3). doi: 10.1029/2009SW000494

1054 Wilks, D. S. (2006). *Statistical methods in the atmospheric sciences* (Second ed.).
1055 Academic Press.